Results in Engineering 29 (2026) 108623

Contents lists available at ScienceDirect

Results in Engineering

journal homepage: www.sciencedirect.com/journal/results-in-engineering

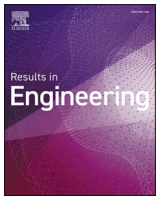

Superhydrophobic bulk ternary and quaternary silicone rubber nanocomposites: An Insight into material selection and performance evaluation

Elham Vazirinasab [a], Khosrow Maghsoudi [a], Gelareh Momen [a,b,*], Reza Jafari [a]

[a] Department of Applied Sciences, University of Quebec in Chicoutimi (UQAC), Chicoutimi, Québec, Canada
[b] Department of Aerospace Engineering, École de Technologie Supérieure, Montréal, Québec, Canada

ARTICLE INFO

Keywords:
Silicone rubber nanocomposites
Durability
Superhydrophobic bulk materials
Icephobicity

ABSTRACT

We developed free-standing superhydrophobic bulk materials without the need for additional surface treatments, demonstrating their potential for commercial applications. The non-wetting properties of the nanocomposites were influenced by various factors, particularly the type, size, and concentration of the embedded particles. A synergic combination of surface roughness and the low surface energy of silicone rubber imparted superhydrophobicy throughout the entire material. To verify consistent bulk water repellency across the bulk, regardless of the incorporated particles, the water contact angle (CA) and contact angle hysteresis (CAH) were measured on both the surface and cross-section of the nanocomposites. To assess suitability for electrical insulation application, thermal properties were evaluated using TGA, while electrical performance was characterized through measurement of dielectric permittivity (Ɛ´), dielectric loss (tan δ), and dry flashover voltage. Icephobicity was examined by measuring both the delay time for the onset of water droplet freezing on the surface and the force required to dislodge a column of ice from the surface. Mechanochemical durability of the produced materials were studied by various means to ensure the long-term performance of the nanocomposites. Finally, to support efficient material selection, radar diagrams were employed to compare the performance of each developed nanocomposite across all evaluation criteria.

1. Introduction

Nowadays, micro-nanostructured surfaces have been considerably employed to fulfill myriad purposes from aesthetic to scientific aspects such as antireflection coatings, biomedical applications, microfluidic devices, flexible electronics, superhydrophobic surfaces, corrosion resistant coatings, etc. [1–7]. According to the literature, micro-nanostructured superhydrophobic surfaces have gained enormous attention owing to their broad range of potential applications including water repellency, self-cleaning, anti-corrosion, anti-fouling, drag reduction, icephobicity, oil-water separation, etc. [7–12]. It is well established that water contact angle (CA) >150° and sliding angle (SA) or contact angle hysteresis (CAH) <10° are two criteria of water-repellent superhydrophobic surfaces on which water droplets can easily roll off. The nature-inspired superhydrophobic surfaces are realized by providing two conditions, i.e., creating micro-nanostructured on the surfaces coupled with possessing low surface energy materials [13].

Fluorinated compounds and silicones are the most prevalent materials used for development of superhydrophobic surfaces [14]. Due to their potential environmental hazards and by-products toxicity for human body, the application of fluorinated compounds has been extensively restricted [15]. Thus, thanks to its low surface energy, silicone rubber can be considered as an ideal alternative for fabrication of superhydrophobic materials.

Recent studies have also shown that the addition of functional fillers such as nanosilica can significantly enhance both the surface and bulk properties of silicone rubber. For example, hydrophilic silica has been shown to transform silicone rubber into superhydrophobic composites, achieving water contact angles above 150° and confirming excellent water repellency [16]. Functionalized nanosilica can also improve mechanical strength while preserving hydrophobicity, which is crucial for durable superhydrophobic materials [17]. Additionally, the inclusion of nanofillers enhances thermal, electrical, and surface stability, particularly under harsh aging conditions such as corona discharge [18].

* Corresponding author.
E-mail address: gelareh_momen@uqac.ca (G. Momen).

https://doi.org/10.1016/j.rineng.2025.108623
Received 18 May 2025; Received in revised form 8 October 2025; Accepted 5 December 2025
Available online 6 December 2025

Wang et al. [8] developed a superhydrophobic surface via deposition of micro-sized aluminum oxide (Al_2O_3) particles on top of the room temperature vulcanized silicone rubber. The CA of $> 150^\circ$ and CAH of $< 10^\circ$, as well as bouncing water droplets on the substrate confirmed its water repellency. Chen et al. [19] created micro-nanostructured silicone rubber surface using a pulsed nanosecond laser. At low laser fluence of 10 J.cm^{-2}, the surface was covered with abundant micro-nanostructures identified by high root mean square value and good water repellency leading to the long freezing delay time and low ice adhesion strength. In a different study, a comparison between micro-nanostructured plasma-treated and replicated superhydrophobic surfaces were accomplished in terms of water repellency, icephobicity, and durability. The larger the surface micro-nanostructures, the longer the freezing delay time and the higher the ice adhesion strength were. It stemmed from the formation of abundant number of air cushions among surface asperities beneath liquid water droplet which reduced the conduction heat transfer and postponed the ice nucleation mechanism, while the frozen water partially trapped within the microstructures increased the ice adhesion strength [20].

In addition, recent research has focused on eco-friendly and high-performance silicone-based coatings. Zwitterion-bearing silica sols were developed by Tan et al. to enhance both the antifouling performance and mechanical strength of PDMS coatings, highlighting the potential of functional nanofillers for multifunctional surface applications [21]. Selim and co-authors developed a series of superhydrophobic and multifunctional silicone-based nanocomposite coatings—mainly using polydimethylsiloxane (PDMS) matrices reinforced with graphene oxide (GO), silver (Ag), titania (TiO_2), and other carbonaceous nanomaterials [22–24]. These studies focused on marine antifouling, icephobic, and self-cleaning surface technologies.

Chen et al. developed passive anti-icing silicone composite coatings, combining anti-icing and photothermal deicing capabilities, further expanding the functional applications of silicone-based materials [25]. In parallel, functionalized rubber nanocomposites have demonstrated superior oil-water separation and mechanical performance. Ghamarpoor et al. incorporated superhydrophobic/silanized silica nanoparticles into nitrile rubber, achieving enhanced oil-water separation efficiency and durability [26,27]. The strategy using silanized nanosilica improved selective oil absorption and water repellency. Functionalization of fillers, such as exfoliated and silanized montmorillonites, was shown to enhance bonding with rubber matrices and improve mechanical performance [26]. Additionally, chemical and photochemical modifications of polymer surfaces, including polyethylene terephthalate fabrics, further improved adhesion and durability in rubber-based nanocomposites [27].

Superhydrophobic silicone rubber surfaces possessing diverse appealing properties such as water repellency, self-cleaning, icephobicity, and anti-corrosion have demonstrated great potential for broad range of applications such as outdoor insulation, aerospace, automobile industry, military industry, and agriculture) [28]. The high-voltage insulators are among the most essential elements in power transmission systems. The functionality of the outdoor insulators can be extremely affected by the ice and pollution accumulation on their surfaces [29]. The combination of accumulated pollution with water or formation of a thin layer of thawed ice on the surface might intensify the conductivity of the surface of insulator. It could lead to the creation of leakage current which may be followed by formation of dry band arcing, and partial electrical discharges, and eventually flash over and power system outage may occur [30,31]. Zhao et al. [32] investigated the effect of different laser-engraved structures on the superhydrophobicity of silicone rubber composite insulators. The optimized diamond column textures surpassed the remained eight different surface structures in terms of superhydrophobic, anti-corrosion, and self-cleaning properties. Wang et al. [33] produced microstructured high-temperature vulcanized (HTV) silicone rubber surface via a simple and cost-effective procedure where the steel mesh patterns replicated on the surface using compression molding procedure. The developed superhydrophobic surfaces showed great self-cleaning, water droplet bouncing, anti-corrosion, and aging resistance. Zhu et al. [34] developed a ZnO/multiwalled carbon nanotube (MWCANT)/PDMS superhydrophobic coating for application to high-voltage insulators. In addition to its self-cleaning superhydrophobic behavior, the coating showed high DC flashover voltage strength, icephobicity and ultraviolet (UV) resistance. One of the common particles used for silicone rubber composite insulators is alumina trihydrate (ATH). ATH could act as a flame retardant agent suppressing the tracking and erosion of silicone rubber [35]. Ribeiro et al. [36] investigated the impact of ATH/SiO_2/-silicone rubber coating on the superhydrophobicity and tracking and erosion resistance of ceramic insulators. The produced superhydrophobic coating showed leakage current $<$60 mA for 2 s indicating its resistivity against tracking and erosion. Room-temperature vulcanized (RTV) silicone rubber was one of the appealing candidates used in superhydrophobic coatings for insulators due to its UV, heat, and weather resistance as well as low electrical conductivity, hydrophobicity and hydrophobic recovery [37]. A two-step procedure was employed to produce a superhydrophobic SiO_2/silicone rubber surface where SiO_2 particles were mechanically scattered on top of the silicone rubber coated substrate [38]. A CA of $\sim$160° and SA of $<5^\circ$ indicated its good water repellency. The coating also showed good stability and water bouncing performance at temperatures up to 200 °C.

Albeit there are numerous studies on the development of superhydrophobic surfaces [34,37,38], their long-term durability against mechanochemical damages is still controversial which can be considered as their Achilles' heel. The segregation of the coatings from substrate, the intrinsic fragility of the surface micro-nanostructures against mechanical damages, as well as the surface chemical reactions with surrounding environment are some examples of unfavorable conditions for superhydrophobic surfaces causing deterioration of their water repellency [39]. To address the short-term durability of the superhydrophobic surfaces, a number of strategies have been proposed such as superior adhesion of coating to the substrate, using mechanical abrasion as a trigger to regenerate the micro-nanostructures, development of self-healing superhydrophobic surfaces, and fabrication of superhydrophobic bulk materials [40–43]. Given the considerable growing demand for damage-tolerant superhydrophobic surfaces, the concept of superhydrophobic bulk materials has been proposed where there is no restriction for superhydrophobicity within the entire bulk materials. Their persistent superhydrophobicity was originated from the presence of low surface energy micro and/or nanoscale particles embedded throughout the bulk as well as the surface [44]. Chen et al. [45] developed a microstructure-controllable superhydrophobic materials based on the 1, 4-conjugated addition reaction. The produced multifunctional organic/inorganic materials possessed diverse characterizations including magnetic-controllable materials for oil-water separation and colored chalk. Liu et al. [46] designed a tunable superhydrophobic bulk material via loading of surface-wrinkled microparticles into the melamine-formaldehyde based porous structure, followed by surface treatment with PDMS. Compared to the pristine sample, the bulk material showed enhanced mechanical properties, superhydrophobic functionality, and effective oil recovery. Although the bulk material achieved appealing mechanical properties as well as oil and organic solvents absorption capacity, it did not possess sliding angle $<10^\circ$ responsible for water repellent materials. Zhang et al. [42] produced super-durable superhydrophobic free-standing material via distributing silica nanoparticles within different polymers with subsequent compression molding of the nanocomposites. However, in order to gain superhydrophobicity, the samples should be manually abraded using sandpaper (SiC, 800 Cw).

In our previous research [47], we developed a non-fluorinated, volumetric superhydrophobic nanocomposite using a simple and cost-effective method. We investigated the effects of embedding diatomaceous earth (DE) and fumed silica (FS) particles into silicone rubber

on the surface and bulk water repellency, hardness and mechanochemical durability of the nanocomposites. The unique porous structure of DE particles, a globally accessible and inexpensive natural mineral, makes them a promising candidate for superhydrophobic materials. In the present study, we focus on the fabrication of ultra-durable, superhydrophobic bulk silicone rubber composites incorporating micro- and nanoparticles for potential use in high-voltage insulator application. To ameliorate the thermal properties as well as tracking and erosion resistance of silicone rubber, the ATH microparticles were added to the material. Micro-scale DE and nano-scale FS particles were used to impart surface and bulk superhydrophobicity. We developed ternary and quaternary ATH/DE/FS/silicone rubber composite and nanocomposites to examine their water repellency, thermal and electrical properties, icephobicity via measuring freezing delay time within a cold chamber and ice adhesion reduction factor (ARF) using a push-off test, and mechanochemical durability.

2. Experimental

2.1. Materials

The produced samples are composed of an HTV silicone rubber matrix filled with embedded particles. Wacker Chemie AG (Germany) kindly provided the high consistency HTV silicone rubber (ELASTOSIL® R 401/60). The curing agent of dicumyl peroxide, microscale DE particles (AW Standard Super-Cel® NF), and Toluene (99 % purity) were purchased from Sigma Aldrich. Surface modified FS with hexamethyldisilazane (HMDS) (AEROSIL® R 812 S) having specific surface area of 195–245 $m^2\ g^{-1}$ was kindly provided by Evonik Industries Co., Germany. Microscale silane treated ATH (Hymod® SB632 SP) with a median particle size of 3.5 μm and specific surface area of 2–5 $m^2\ g^{-1}$ was kindly supplied by Huber Engineered Materials Co., USA.

2.2. Sample preparation

The preparation procedure is comprised of two complementary steps including distribution of the particles within HTV silicone rubber via solution mixing approach and curing the produced compound using compression molding system (Carver Inc., USA). First, 12 g silicone rubber was added into 100 mL toluene and the solution was stirred for 2 h using an overhead stirrer to have a homogenous solution. Each of the particles were separately dispersed in toluene for 100 min using ultrasonication and magnetic stirrer to ensure uniformity. Then the produced suspensions having various weight fractions were sequentially added to the silicone rubber solution with the following order of DE, FS, and ATH. The mixture was blended for 100 min at 75 °C before the addition of second and/or third suspension. Eventually, 0.09 g of dicumyl peroxide was dissolved within the compound for 20 min at room temperature. In order to eliminate the residual toluene, the produced compound was left at room temperature under vacuum for 24 h. The final preparation step is curing in a compression molding machine under 20 MPa pressure for 6 min at 175 °C [47].

2.3. Characterization

We employed a Kruss™ DSA100 goniometer to assess the water repellency of the intact surface of materials and their cryogenically fractured cross-section. Using the Young-Laplace approximation, the water CA and CAH were measured by deposition of 4-μL deionized water droplet on the intended surface at room temperature. The CAH was described as the difference between advancing and receding contact angles of a moving 4 μL water droplet. The chemical composition of the developed samples was identified using a Cary 630 (Agilent, USA) attenuated toral reflection- Fourier transform infrared (ATR-FTIR) spectroscopy. The surface roughness of the samples was observed with scanning electron microscopy (SEM) using JSM-6480 LV, and it was quantified with the help of an optical profiler (Profil3D, Filmerics).

The swelling experiment was performed based on the ASTM D6814 –02 to study the impact of incorporated particles on the crosslink density of the produced materials. The swelling ratio (Q), volume fraction of the silicone rubber in the swollen specimen (ϕ), Flory-Huggins parameter for polymer-solvent interaction (χ) crosslink density (ν), and average mass between the adjacent crosslink points (M_C) can be calculated as follows:

$$Q = \frac{m_1 - m_2}{m_2}$$

$$\phi = \frac{\left(\frac{m_2 \times b}{\rho_r}\right)}{\left(\frac{m_2 \times b}{\rho_r}\right) + \left(\frac{m_1 - m_2}{\rho_s}\right)}$$

$$\chi = 0.459 + 0.134\phi + 0.59\phi^2$$

$$\nu = \frac{-\left(\ln(1-\phi) + \phi + \chi\phi^2\right)}{V\left(\phi^{\frac{1}{3}} - \frac{\phi}{2}\right)}$$

$$M_C = \frac{\rho_r}{\nu}$$

Where m_1, m_2, b, ρ_r, ρ_s, and V are the weight of swollen sample in toluene, the weight of swollen sample after drying, the weight fraction of rubber, the density of rubber (1.15 g cm^{-3}), the density of toluene (0.87 g cm^{-3}), and the molar volume of toluene (106.7 $cm^3\ mol^{-1}$), respectively. Moreover, the hardness values which were the average of six repeated measurements on each sample were obtained using a shore A durometer (2000 max hand durometer, Rex Gauge).

The thermogravimetric analysis (TGA) was conducted to study the thermal properties using a SETSYS Evolution TG/DTA 24 (Setaram, France). All samples were heated from 50 °C to 700 °C with the heating rate of 20 °C min^{-1} under nitrogen atmosphere. The dielectric properties of the samples were measured by a broadband dielectric spectrometer (Novocontrol) over the frequency range of 10^{-1} Hz to 10^5 Hz. To determine the flashover voltage, the experimental set-up was designed as a rod-plate electrode configuration under AC voltage. To this end, the voltage was increased quickly up to 20 kV where no apparent discharge activity was observed, then the voltage was risen at constant rate of 0.5 kV s^{-1} until formation of the first complete discharge. After two-minute pause, we repeat the exact procedure for 10 times on the selfsame sample.

Among diverse application of superhydrophobic surfaces, we studied the icephobic behavior of produced materials via measuring their freezing delay time within a cold chamber and ice adhesion reduction factor (ARF) using push-off test. As its name implies, the freezing delay time indicates the exact time it takes a water droplet to initiate freezing on the supercooled surfaces. We measured the freezing delay of the samples at −15, −20, and −25 °C. To determine the ice adhesion strength of the materials, we measured the shear stress required to detach a cylindrical ice column frozen onto the surface using a force gauge. To have an ice cylinder on the surface, we filled a 1-cm diameter plastic mold set onto the substrate with deionized water and placed them inside a cold chamber at −10 °C for 24 h. The shear force was measured by pushing the ice column toward the force gauge at a constant speed of 0.05 mm s^{-1}. Then, the ice adhesion strength and ARF were calculated by dividing the maximum shear force at the detachment point to the surface area of the ice column, and the ice adhesion strength of the produced materials to that of pristine silicone rubber, respectively.

We performed comprehensive mechanochemical durability analyses including sandpaper abrasion, tape peeling, cutter scratching, dynamic impact tests, immersion, and UV resistance. The abrasion durability is

performed by pulling the materials along sandpapers with various grit numbers (i.e., from rough to fine #320, #800, and #1200) carrying a constant pressure of 10 kPa (Manual Clemen Unit, Elcometer 3000, USA). The water CA and CAH of the abraded samples were measured after dragging the samples along the sandpaper for 5000 cm. The durability of the materials against peeling was assessed by adhering a transparent Scotch tape to the surface under a constant 1 kPa force and then peeling it off the surface. We performed the adhesion/ peeling cycle for 150 times and then the surface water CA and CAH were measured. The surfaces were also subjected to multidirectional scratching using a brand-new cutter blade to assess their stability to the deep randomly applied scratches. The dynamic impact test is divided into liquid and solid analyses which was performed on the DE80/ATH100 composite. In liquid impact test, a stream of deionized water runs over the surface tilted at 40° for 10 min. The reservoir was placed 30 cm above the surface. Regarding solid impact durability test, the tilted sample was bombarded with 200 g of 50-μm silicon carbide (SiC) particles from the same height, i.e., 30 cm. The contaminated surface got cleaned with a water jet using a 5-mL syringe.

The immersion is a severe test to examine the chemical durability of the materials submerged in acidic (pH = 4), neutral (pH = 7), and alkaline (pH = 10) solutions for 48 hrs. As another viable durability assessment for materials designed for outdoor applications, we studied the ultraviolet (UV) resistance of the produced materials with a QUV-accelerated weathering test. The samples were subjected to the UVA-340 fluorescent lamps with a radiation energy of 0.89 W m^{-2} at 70 °C for 300 h. Eventually, in order to examine the hydrophobic recovery ability of the materials, the surface of the materials was exposed to 20-times subsequent flashovers. The alteration in the water repellency of the materials was monitored for 20 days.

3. Results and discussion

3.1. Superhydrophobic functionality and surface characterization

To ensure the bulk water repellency of the samples, regardless of the incorporated particles, the water CA and CAH of the surface and cross-section of the nanocomposites were measured. As shown in Table 1, the water CA and CAH values of the produced composites met the criteria of superhydrophobic materials causing the water drop to bead up as a typical sphere on their surface. Although all the materials demonstrated the superhydrophobic behavior, the nanocomposite DE80/FS30/ATH100 possessed highest water CA and lowest CAH indicating the favorable impact of hierarchical micro-nanostructures on the water repellency. While the DE and ATH particles were responsible for micro-scale roughness, the FS contributed to the creation of nano-scale features. The presence of DE micro-particles is staple for having superb surface and bulk water repellency. By replacing FS particles with DE, the surface water CA noticeably enhanced from 153.2° to 162.5° and surface CAH reduced from 7.6° to 3.2°

Fig. 1 demonstrates the encircling water around superhydrophobic nanocomposite surface, bouncing a water jet off the surface, bulk superhydrophobicity, a complete rebound of a 20-μL water droplet, and an intense contact of a 10-μL water droplet on the superhydrophobic DE80/FS30/ATH100 nanocomposite. Fig. 1(A) shows the water repellent behavior of the surface prevented the surrounded water to flow over the surface and thoroughly immerse it. The freestanding ~5-mm-height water wall encircled the nanocomposite indicates the superb ability of the surface to keep water away. As shown in Fig. 1(A) inset, a strong water jet easily bounced off the surface leaves behind no visible trace or alteration in surface appearance. Fig. 1(B) shows the water wall receding from all around the bulk superhydrophobic nanocomposite. The bouncing behavior of a 20 μL free-falling water droplet onto the surface is illustrated in Fig. 1(C). When the drop released from 3 cm above the surface came in contact with the surface, it underwent all three successive stages of spreading, retraction, and rebounding within 20.0 ms. Thus, the water drop can be easily detached from the surface without leaving any traces which confirms the low adhesion of the surface with water. On the other hand, considering the size and fragility of the surface micro-nanostructures, they might not withstand the penetration of pressed water droplet which results in its stiction to the substrate. Despite the applied pressure on the water droplet with a needle, the water maintained its quasi-spherical shape during tight and intense contact. The untouched shape of water droplet during compression with its subsequent effortless detachment from the surface indicated the substantially low adhesion between the water droplet and superhydrophobic surface (Fig. 1(D)).

The FTIR and SEM analyses illustrate the altered surface chemical composition as well as the surface morphology of the materials by incorporation of diverse particles (Fig. 2). The considerable resemblance of DE and FS absorption spectra verifies the silica-based chemical composition of DE particles (Fig. 2(A-1)). The absorption spectrum at ca. 795 and 1015 cm^{-1} are respectively attributed to in-plane Si-O stretching and symmetric Si-O stretching [48]. For HMDS-treated FS particles, there are also two diminutive absorption peaks at 1420 and 2960 cm^{-1} characterize the stretching and bending modes of C—H in CH_3. By incorporation of the particles within materials (Fig. 2(A-2)), the distinguished difference between their absorption peaks and pristine HTV silicone rubber is located at ca. 3250–3650 cm^{-1} corresponded to the hydroxyl (-OH) groups within ATH particles [48]. Nevertheless, all three samples show relatively identical absorption bands. The strong absorption peak centered at ~1015 cm^{-1} is attributed to Si-O-Si band. The sharp spectra located at 790 cm^{-1} along with its two small shoulders at ca. 750 and 860 cm^{-1} are assigned to Si-alkyl groups such as $Si(CH_3)_2$ and $Si(CH_3)_3$ [50]. The remained spectrum at ca. 1260, 1420, and 2960 cm^{-1} characterize the $Si(CH_3)$, CH_3 in $Si(CH_3)$ and CH in CH_3 [50,47].

As the second prerequisite of superhydrophobic materials, the impact of micro-nanoparticles on the nanocomposites surface morphology was studied using SEM analyses (Fig. 2(B) and Fig. 3). The pristine HTV silicone rubber seemed to be somewhat smooth having no noticeable surface structures (Fig. 2(B-1) and Fig. 3(A)). In relative to pristine silicone rubber, all three samples showed higher surface roughness. The substrate of composite DE80/ATH100 (Fig. 2(B-2) and Fig. 3(B)) was predominantly composed of uniformly dispersed micro-sized different-shaped porous DE particles which is in favor with the advanced water repellency. The nanocomposite FS8/ATH100 appeared to be covered with smaller and regular roughness features resembling the aggregated granular-shape structures (Fig. 2(B-3) and Fig. 3(C)). However, the great superhydrophobic functionality of nanocomposite DE80/FS30/ATH100 indicates the prominent role of embedded DE particles in producing multiple protrusions and depressions on the surface in addition to the nanoscale FS superimposed on DE particles responsible for more distinct nanostructures (Fig. 2(B-4) and Fig. 3(D)).

Table 1
Water CA and CAH of the pristine silicone rubber and various produced composites.

Nanocomposite	DE (phr)	FS	ATH	Surface		Bulk	
				CA (°)	CAH (°)	CA (°)	CAH (°)
Pristine silicone rubber	-	-	-	110.0 ± 1.7	49.1 ± 2.9	111.8 ± 2.2	48.9 ± 3.1
DE80/ATH100	80	-	100	161.7 ± 2.3	3.3 ± 0.4	158.2 ± 2.0	4.7 ± 0.5
FS80/ATH100	-	80	100	153.2 ± 1.4	7.6 ± 1.1	152.1 ± 1.5	5.4 ± 1.2
DE80/FS30/ATH100	80	30	100	162.5 ± 2.5	3.2 ± 0.6	160.8 ± 1.8	3.5 ± 0.4

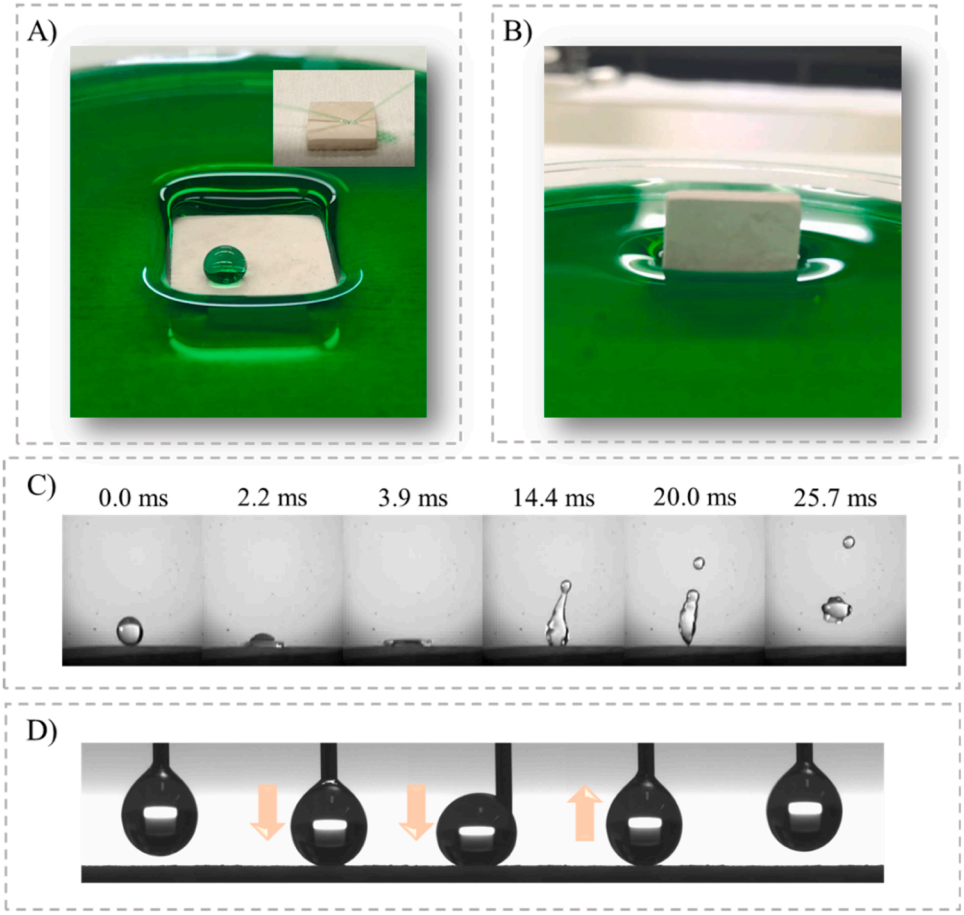

Fig. 1. A) the encircling water around superhydrophobic nanocomposite surface and bouncing a water jet off the surface; B) demonstration of bulk superhydrophobicity; C) the complete rebound of a 20-μL water droplet from the superhydrophobic surface; D) an intense contact of a 10-μL water droplet on the superhydrophobic DE80/FS30/ATH100 nanocomposite.

3.2. Equilibrium solvent swelling, crosslink density and hardness properties

One of the fundamental structural and physical attributes of rubber materials is entitled "crosslink density" which is defined as the density of the crosslink bonds connecting two parts of a polymer network per unit volume [51]. The Equilibrium solvent swelling is a conventional technique to determine the crosslink density and subsequently the average molecular weight between two crosslink segments (M_C). The swelling ratio is inversely proportional to the crosslink density. The higher the swelling ratio, the more elongated polymeric chains and greater number of free volumes are. Thus, the higher swelling ratio identifies a crosslinked rubber network having low crosslink density and high M_C [52]. The crosslink density as well as hardness value of the composite DE80/ATH100 is the highest among the produced materials and pristine silicone rubber (Table 2). The improved crosslink density could be ascribed to two chemical and physical interactions including the interfacial interactions between siloxane groups of DE particles and silicone rubber, and increased amount of crosslinked bonds formed within the rubber network [47]. Moreover, the synergistic effect of increase in crosslink density as well as the great amount of incorporated elastic solid phase can considerably reinforce the hardness of the composite.

Although the crosslink density of the nanocomposites FS80/ATH100 and DE80/FS30/ATH100 was respectively 32 % and 24 % less than that of HTV silicone rubber, their hardness values demonstrated respective enhancement of 48 % and 55 %. The restricted movement of rubber chains in the presence of nano-sized FS particles located among them could reduce the crosslink formation and crosslink density. However, the considerable number of solid particles along with the limited movement of silicone rubber chains by embedded FS particles are in favor of hardness enhancement in these nanocomposites.

3.3. Thermal and electrical properties

Among various destructive conditions such as ozone, corona, UV, and heat, local heat accumulation is the dominant factor causing thermal degradation and loss of hydrophobicity in silicone rubber materials which trigger dry band arcing [53]. Thus, thermal stability of the insulating materials has a considerable impact on their carbonized tracking and erosion resistance [54]. According to the literature, ATH-filled silicone rubber composites showed enhanced flame retardancy as well as tracking and erosion [55,35]. Carbon formation and volatilization are the two processes determine the carbonized tracking of polymer insulating materials. The faster rate of carbon volatilization than carbon formation surpasses the tracking [56]. At high temperature, ATH particles start an endothermic decomposition to form water molecules which dissipate the generated heat and retard the flame propagation. Moreover, the released water molecules can react with methyl side-groups instead of siloxane groups on the backbone of silicone rubber chains leading to the formation of CH_4, and CO_2 gases as well as SiO_2. Consequently, fewer silicone oligomers as well as fewer carbon produced in the composite result in enhancement of tracking and erosion resistance of silicone rubber [57].

In this section, TGA analyses were employed to comprehend the effect of incorporated particles on the thermal stability of the filled silicone rubber nanocomposites. As shown in Fig. 4, two TGA attributes are

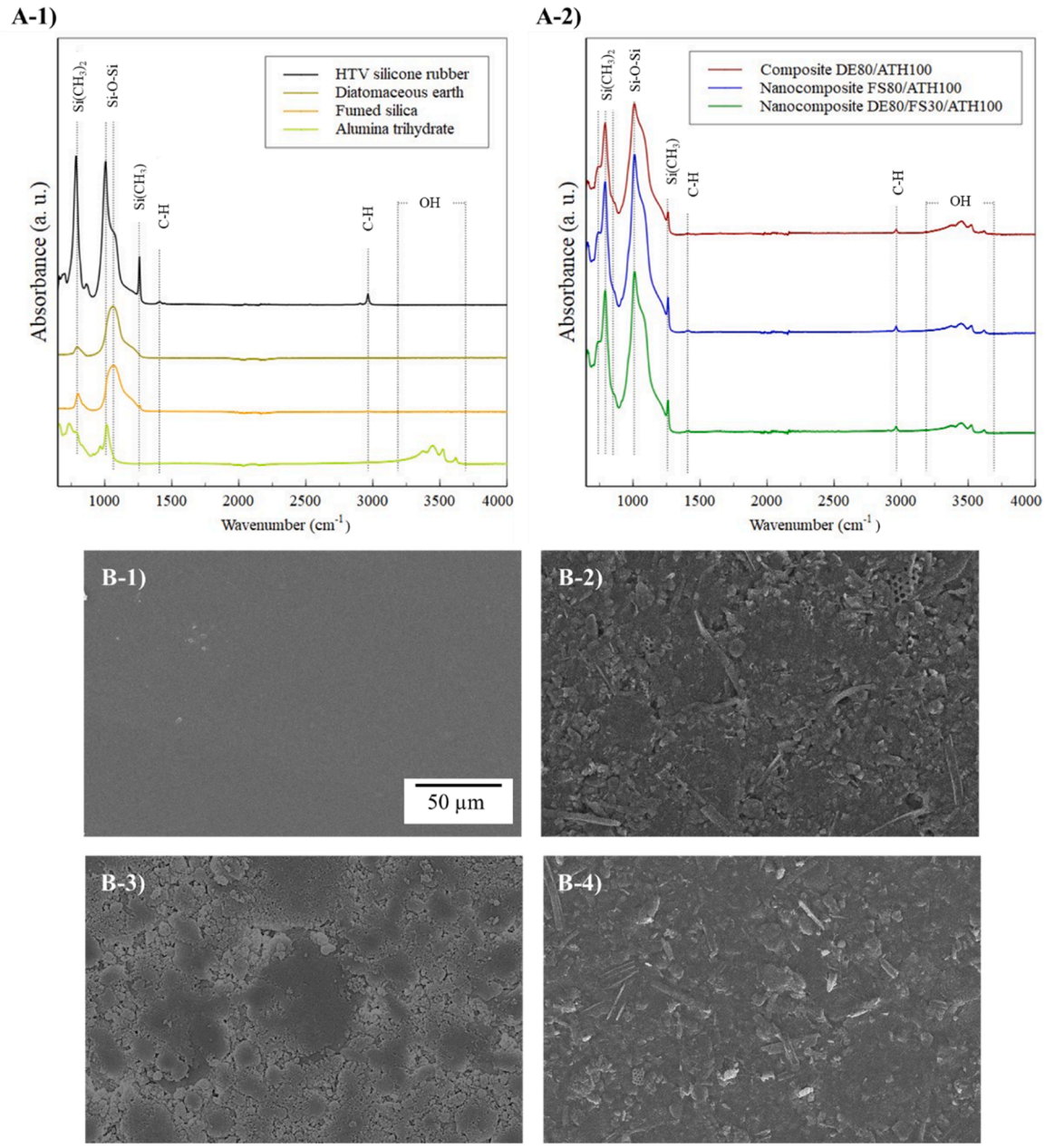

Fig. 2. A) FTIR spectra of A-1) pristine HTV silicone rubber, DE, FS, and ATH; A-2) composite DE80/ATH100, nanocomposite FS80/ATH100, and nanocomposite DE80/FS30/ATH100. B) SEM images of B-1) pristine HTV silicone rubber, B-2) composite DE80/ATH100, B-3) nanocomposite FS80/ATH100, B-4) nanocomposite DE80/FS30/ATH100.

$T_{10\ \%}$ and $T_{50\ \%}$ which represent the corresponding temperature to lose 10 % and 50 % weight of the samples, respectively. Under argon gas flow as a neutral environment, the unfilled silicone rubber was decomposed to its cyclic oligomers at the temperature range of 400–580 °C. A two-step weight loss process was identified for the produced nanocomposites which initiates with dehydration of ATH particles followed by decomposition of silicone rubber and coupling-agents. Within the temperature range of 260–360 °C, the primary stage of weight loss was occurred due to the water releasing process from ATH particles during which they were converted into alumina (Al_2O_3) particles. Consequently, the $T_{10\ \%}$ of developed materials was considerably lower than that of pristine silicone rubber. Having an equal amount of ATH particles, the weight reduction during the first stage was similar for all three of them (~15 %). However, the second peak was the most significant weight loss for the produced materials. Considering the superb thermal stability of each of these inorganic particles at temperatures below 800 °C, the second weight loss can be ascribed to the decomposition of silicone rubber chains along with organic coupling agents on FS and ATH particles which can be considered as the origins of the two-shoulder peaks of the second derivative weight loss (Fig. 4(B)). Interestingly, by the incorporation of DE particles, the second weight loss step was initiated at higher temperature (~460 °C) than nanocomposite FS80/ATH 100, i.e., ~370 °C, and a broadened range of decomposition temperature with lower weight loss rate was observed. These observations verified the improved thermal stability of the materials containing micro-scaled DE particles. Under inert gas environment, the water molecules were expected to accelerate the hydrolysis process of silicone rubber chains at high temperatures resulting in decomposition of ATH-filled materials at lower temperature compared to pristine silicone rubber [58]. Although the nanocomposite FS80/ATH100 followed the expected trend, the thermal stability of the DE containing nanocomposites was noticeably enhanced. It can justify the chemical

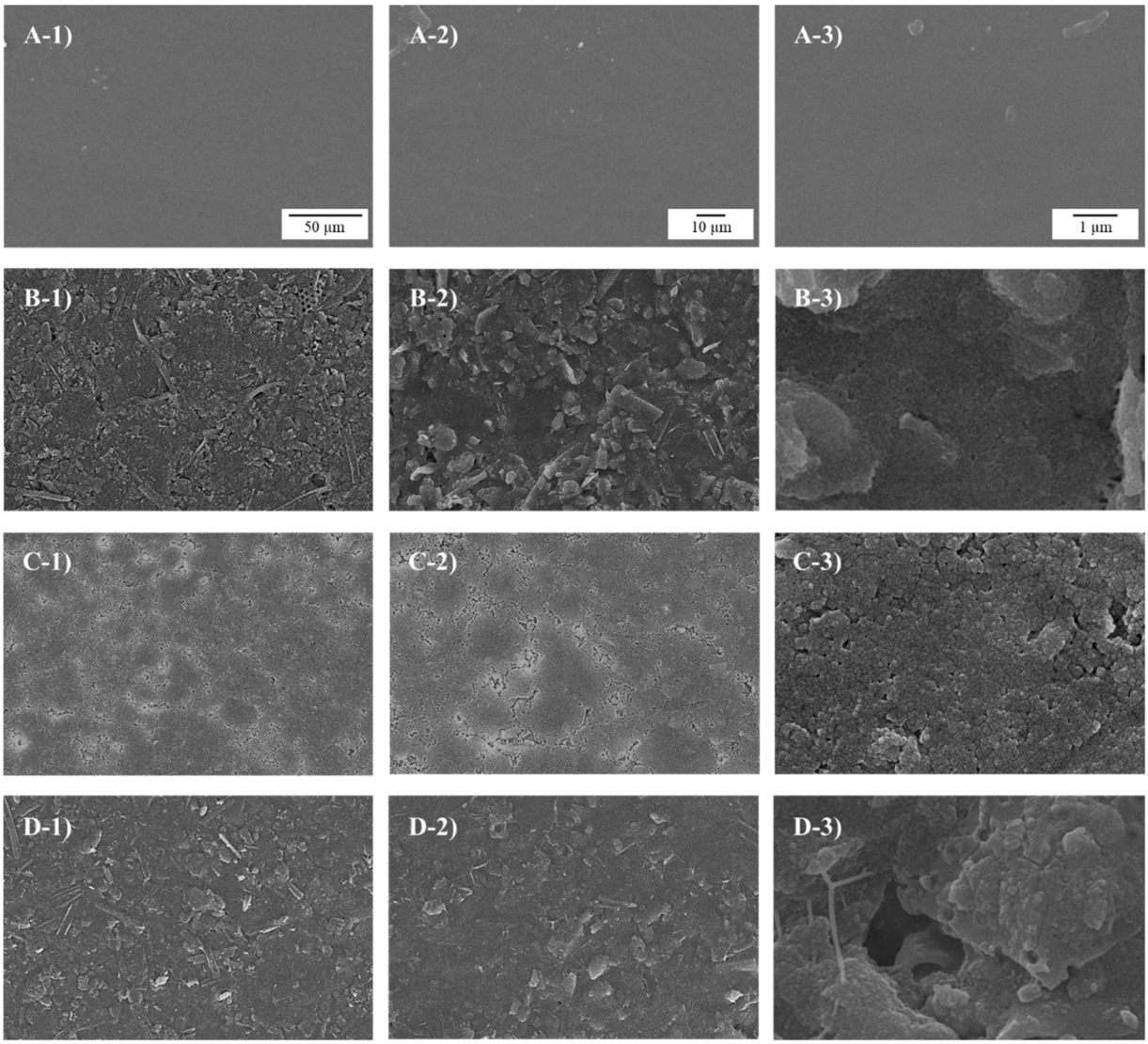

Fig. 3. SEM images of A) pristine HTV silicone rubber, B) composite DE80/ATH100, C) nanocomposite FS80/ATH100, D) nanocomposite DE80/FS30/ATH100, at various magnifications.

Table 2
The swelling ratio, crosslink density, average molecular weight between two crosslink segments (M_C), and hardness of the produced samples.

Type	Swelling ratio	Crosslink density (mol cm^{-3}) × 10^{-4}	M_C (g/mol)	Hardness (Shore A)
HTV Silicone rubber	1.485 ± 0.002	1.63 ± 0.02	7076 ± 109	62.8 ± 0.7
DE80/ATH100	0.515 ± 0.003	1.70 ± 0.04	6775 ± 237	98.5 ± 0.7
FS80/ATH100	0.612 ± 0.007	1.10 ± 0.07	10,430 ± 429	93.1 ± 0.3
DE80/FS30/ATH100	0.566 ± 0.004	1.24 ± 0.06	9249 ± 271	97.6 ± 0.8

reactions of the methyl side-groups of silicone rubber with siloxane groups of DE particles which postpone the thermal degradation of silicone rubber chains. Moreover, it is worth mentioning that given the significant amount of embedded inorganic particles in the nanocomposites, >50 % residue of the produced materials remained at 650 °C.

The dielectric parameters, which can be measured by broadband dielectric spectroscopy, represent the physical characteristic of the dielectric materials like their polarization and loss performance [59]. Fig. 5 (A and B) demonstrates the alteration in dielectric permittivity (ε′) and dielectric loss (tan δ) of HTV silicone rubber by the incorporation of particles and their frequency dependency. The frequency-independent low dielectric constant of pristine HTV silicone rubber stems from its relatively low molecular polarity and rapid segmental dipole polarization. Thus, its low dielectric loss is also attributed to the limited electrical energy dissipation during polarization [60]. Compared to pristine silicone rubber, all three samples possess higher dielectric permittivity and dielectric loss because of their inherently higher dielectric constant. In general, the discrepancy in dielectric permittivity of silicone rubber and embedded particles can distort the electrical field distribution of material causing Maxwell-Wagner interfacial polarization and interfacial charge trapping [61,62]. High dielectric constant of ATH prompts the space charge accumulation trapped within particle-matrix interface. The consequential interfacial polarization will intensify the dielectric permittivity and dielectric loss values of the nanocomposites simultaneously, specifically at low frequencies [63]. It can be seen that the impact of embedded particles is more pronounced at frequencies <10 Hz where the nanocomposite

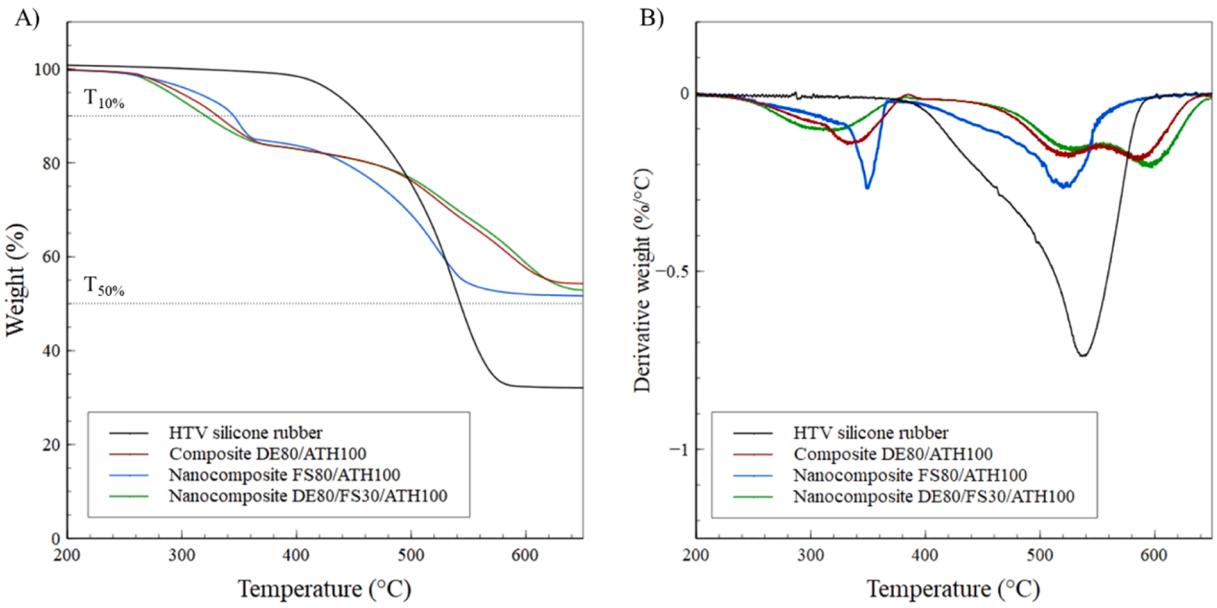

Fig. 4. TGA graphs of the HTV silicone rubber and the produced samples.

FS80/ATH100 shows the lowest dielectric permittivity and dielectric loss values of all materials. The compatibility of the silane-treated FS particles and their acceptable dispersion within silicone rubber matrix can result in the reduced dielectric permittivity and dielectric loss due to the following justifications: firstly, the lower interfacial polarization and accumulated space charge at the FS-rubber interface, and secondly, the restricted movement of silicone rubber chains trapped among dispersed nanosized FS particles with considerably high surface area which may result in by reduction in the dipole polarization of their chains [60].

Due to the functionality of the insulators under natural outdoor conditions, some might undergo elevated temperatures. Therefore, we also examined the dielectric loss of nanocomposites at various temperatures from 30 °C to 60 °C. Fig. 5C demonstrates relatively negligible changes of their dielectric loss over temperature at the specific power frequency of 1 kHz. At higher temperature, the increased mobility of the chains facilitates dipole rotation, leading to greater dielectric loss [58]. In the absence of nanosized FS particles, the relative enhancement of the dielectric loss over temperature is slightly higher than FS-filled nanocomposites.

The impact of embedded particles on the dry flashover voltage of nanocomposites was studied as well (Fig. 5(D)). The experiments were conducted under environmental conditions where AC voltage with ramping rate of 0.5 kV/s was applied to the materials. Regardless of the type of particles, all three materials possessed higher dry flashover voltage than HTV silicone rubber. It was found that the composite DE80/ATH100 attained the highest flashover voltage of 28.27 ± 0.62 kV proportional to ~12 % enhancement compared to that of pristine HTV silicone rubber (25.20 ± 1.38 kV). Considering the relatively similar chemical composition of the FS and DE particles, these results can be chiefly attributed to the surface roughness of the nanocomposites. The higher the surface roughness, the better the surface flashover voltage is. This observation is consistent with the results presented in [64] where at surface roughness >3 μm, the flashover voltage was enhanced with increasing roughness. Therefore, these observations indicated the enhanced insulation strength of the nanocomposites.

Additionally, the alteration in the flashover voltage of the pristine silicone rubber and the nanocomposites was examined over ten consecutive tests (Fig. 5D). Although the flashover voltage of pristine silicone rubber gradually declined with the number of consecutive tests, that of nanocomposites remained relatively unchanged after ten successive tests. Owing to the higher dielectric permittivity of the nanocomposites than pristine, the residual charges produced through the previous flashovers were rapidly emitted. Thus, the distortion in their electric field distribution was prevented resulting in stable flashover voltage [34].

3.4. Dynamic water droplet impact

The dynamic behavior of water droplet impact against superhydrophobic surfaces is a vital parameter for materials designed for outdoor applications. We videotaped the bouncing behavior of a 20 μL water droplet free fallen from a height of 3 cm above the substrate using a high-speed camera. Due to its relatively high surface energy, the water droplet adheres to the pristine HTV silicone rubber when it comes in contact with it. While, spreading, retraction, and rebounding are three subsequent stages that a bouncing water droplet follows on a water-repellent substrate (Fig. 6(A)). Comparing to the pristine silicone rubber, the water droplet undergoes shorter spreading time on the superhydrophobic surfaces owing to its lower surface energy (Table 3). Due to its smaller surface roughness, it takes longer time for the water droplet to spread on the surface of nanocomposite FS80/ATH100 than other developed materials. Albeit the difference in the spreading time, the water droplet can simply rebound the superhydrophobic surfaces after ~20–28 ms. The droplet experiences full bouncing cycle on all the produced materials without leaving any water attached to the surface. These observations identify the appealing dynamic water repellency of the composite and nanocomposites verifying the persistence of the Cassie-Baxter regime against falling water droplet. To gain a better understanding of dynamic behavior of water droplet, the alteration of spreading factor (D*) over time is illustrated in Fig. 6(B). The spreading factor is defined as the diameter of water droplet during impingement process (D′) over its initial diameter (D) (D*=D′/D) [65]. Through impinging, the spreading and deformation of water droplet stems from an energy transformation from kinetic to surface energy [49]. Corresponding to the substrate attributes, the surface energy of the droplet can be fully or partially dissipated which affects its following retraction and/or rebounding steps. The lower the energy dissipation, the more energy is restored within the droplet which enhance the probability of its rebounding stage [64]. Compared to the ternary materials, the quaternary nanocomposite DE80/FS30/ATH100 showed smaller spreading factor and shorter contact time which can be ascribed by its better water repellency. Consequently, the shorter contact time of water droplet on

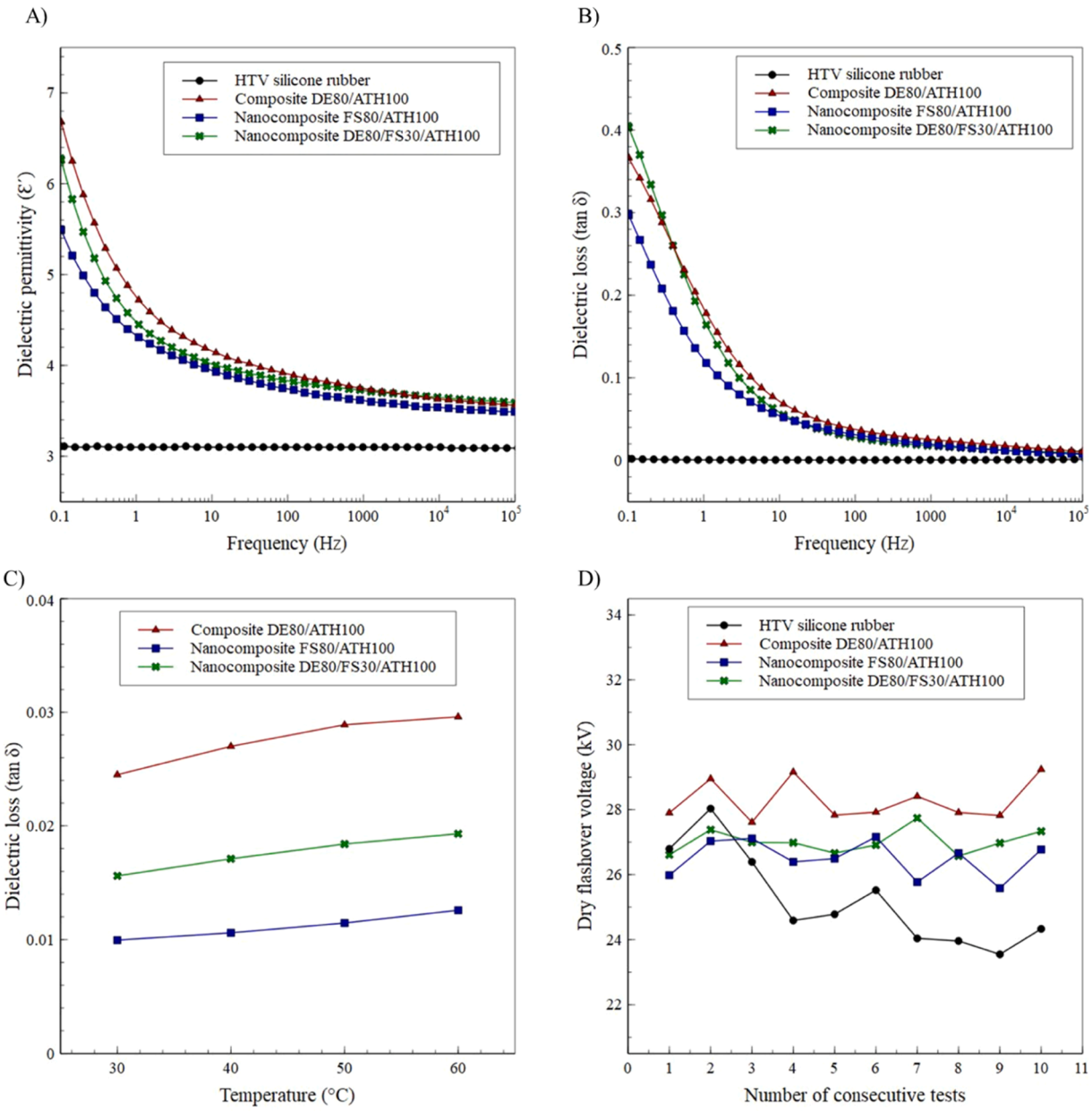

Fig. 5. A) Dielectric permittivity and B) dielectric loss as a function of frequency; C) Dielectric loss at various temperatures; D) Dry flashover voltages of HTV silicone rubber and the produced materials.

the nanocomposite DE80/FS30/ATH100 and composite DE80/ATH100 verifies their lower energy dissipation than nanocomposite FS80/ATH100 which leads to a greater number of bounces (i.e., five and four bounces were observed on these surfaces respectively).

3.5. Icephobicity

Hitherto, several strategies have been proposed to eliminate and avert the ice formation and/or accumulation on the surfaces utilized in outdoor conditions. They can be categorized into two distinct groups: 1) active de-icing approach where de-icing chemicals and/or external mechanical, thermal, and electrical energy sources are employed to remove the accreted ice; 2) passive anti-icing methods whereby controlled substrate properties postpone or avert the ice formation, and/or mitigate the ice adhesion strength which considerably facilitate the further icing removal process without any external forces [66,67]. Given the high cost, energy-demanding, time-consuming and environmental concerns of the active de-icing approaches, the passive anti-icing methods have received tremendous attentions among which fabrication of superhydrophobic surfaces having high water repellency is one of the facile yet promising methods [20].

The freezing delay and ice adhesion strength measurements give insight into the anti-icing performance of the developed superhydrophobic surfaces. The freezing delay analysis measures the time it takes for a water droplet to freeze on a surface at subzero temperatures [65]. Thus, the longer delayed in the freezing process, the better anti-icing properties the surface have. There are various factors controlling the freezing process of a water droplet such as surface roughness, thermal conductivity of the substrate, temperature, and environmental humidity [68]. Under constant environmental conditions, creation of favorable surface roughness can considerably enhance the water freezing time. As shown in Fig. 7(A), all micro-nanostructured superhydrophobic surfaces possessed longer freezing delay time than silicone rubber at different temperatures. In comparison to HTV silicone

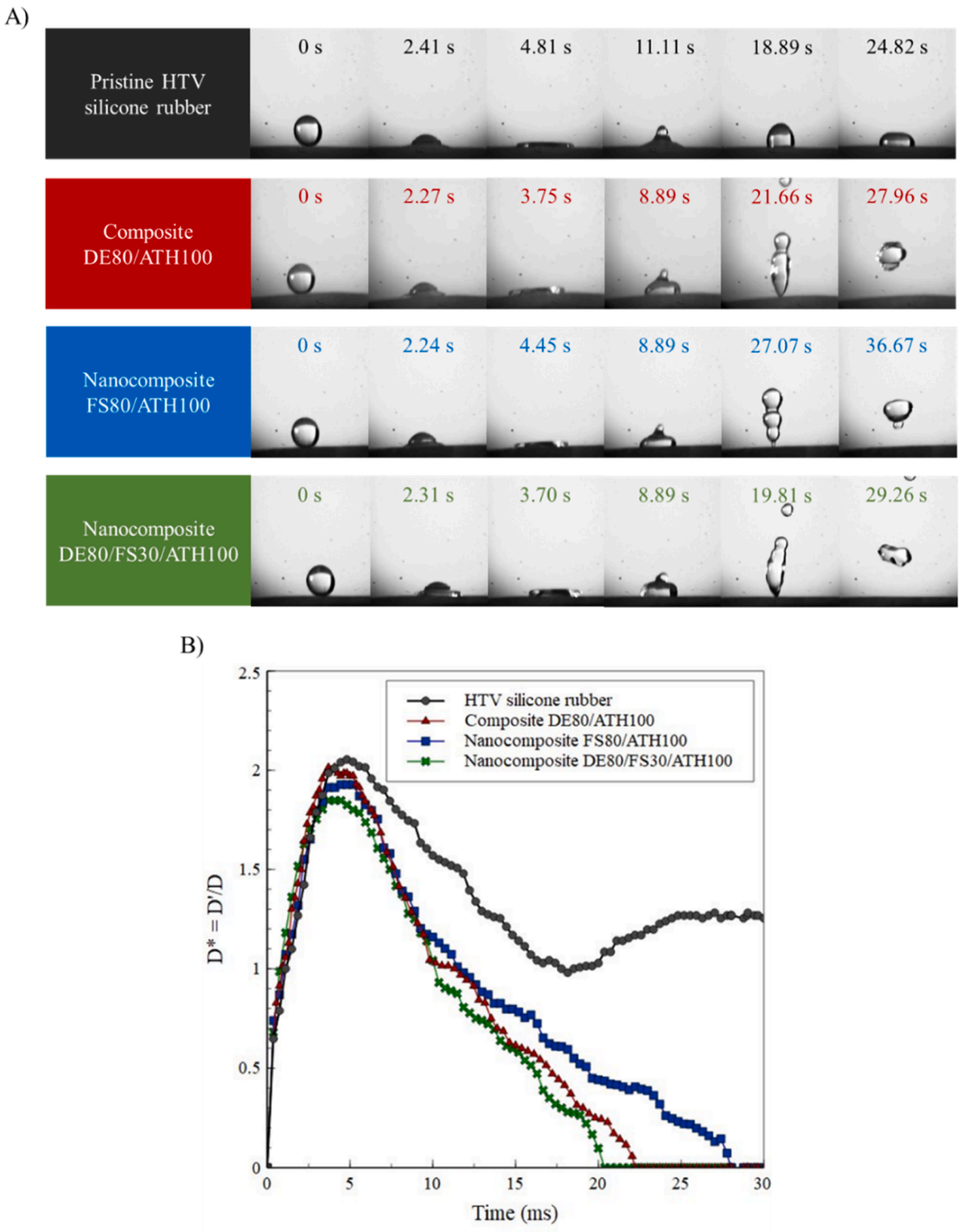

Fig. 6. A) Snapshots of the stages of water droplet impacting various samples; B) alteration of spreading factor (D*) over time.

rubber, the freezing time on the nanocomposite DE80/FS30/ATH100 was ~3 times longer. At −20 °C, it took ~570 s for the water droplet to freeze on a pristine silicone rubber, whereas it needed ~1580 s to congeal on the nanocomposite DE80/FS30/ATH100. Even at lower temperature, i.e., −25 °C, the freezing delay on this nanocomposite was ~680 s which was twice the required freezing time for pristine surface. The limited droplet-substrate contact area on the superhydrophobic surfaces can not only reduce the conduction heat transfer but retard the heterogenous nucleation and growth process. In addition, the presence of air cushions confined among the surface asperities beneath the water droplet prevents convection heat transfer that results in longer freezing delay [69]. Moreover, considering its hierarchical micro-nanostructured surface roughness, the nanocomposite DE80/FS30/ATH100 was identified with the longest time required for freezing process than other nanocomposites.

Moreover, given the greater thermal conductivity of the inorganic particles than silicone rubber specifically ATH particles owing to their metallic nature [70], it was expected to observe shorter water freezing

Table 3
Dynamic water droplet impact values on HTV silicone rubber and the produced samples.

	Time of spreading (ms)	Time of rebounding (spreading + retraction) (ms)	Number of bounces
HTV silicone rubber	4.81	-	-
Composite DE80/ ATH100	3.75	22.04	4
Nanocomposite FS80/ ATH100	4.45	27.77	2
Nanocomposite DE80/ FS30/ATH100	3.70	20.00	5

time on the nanocomposites. Nevertheless, the freezing time was prolonged by the incorporation of the particles due to the induced micro-nanostructures on the surface of the nanocomposites (Fig. 7(A)).

To evaluate the anti-icing performance of the produced materials, we employed a push-off system to assess the ice adhesion strength of the developed nanocomposites at −10 °C. We performed 5 consecutive push-off measurements on each sample to ascertain the consistency of their anti-icing properties. The icephobicity of the materials is inversely proportional to their ice adhesion strength, i.e., the lower the ice adhesion strength, the better the icephobic properties are. To have a better understanding on their comprehensive icephobic performance against pristine HTV silicone rubber, the ARF values were defined as the ratio between ice adhesion strength of the silicone rubber to that of composite and nanocomposites (Fig. 7(B)). The ice adhesion strength of the pristine surface is ~131 kPa. While it reached the lowest amount of ~35 kPa on the quaternary nanocomposite DE80/FS30/ATH100 which is equivalent to the ARF of ~3.7. It can be seen that by the incorporation of particles, the ARF values were enhanced due to the formation of micro-nanostructures on the surface. The lack of FS particles within the DE80/ATH100 composite results in the lowest ARF value (~3) indicating the undeniable impact of nanostructures superimposed on top of the micro features on the icephobic properties. The differing results of the three samples stem from the presence of nano-features on the surfaces as well as the possibility of the ice interlocking among the surface micro-features. In addition, we observed that the ARF values are

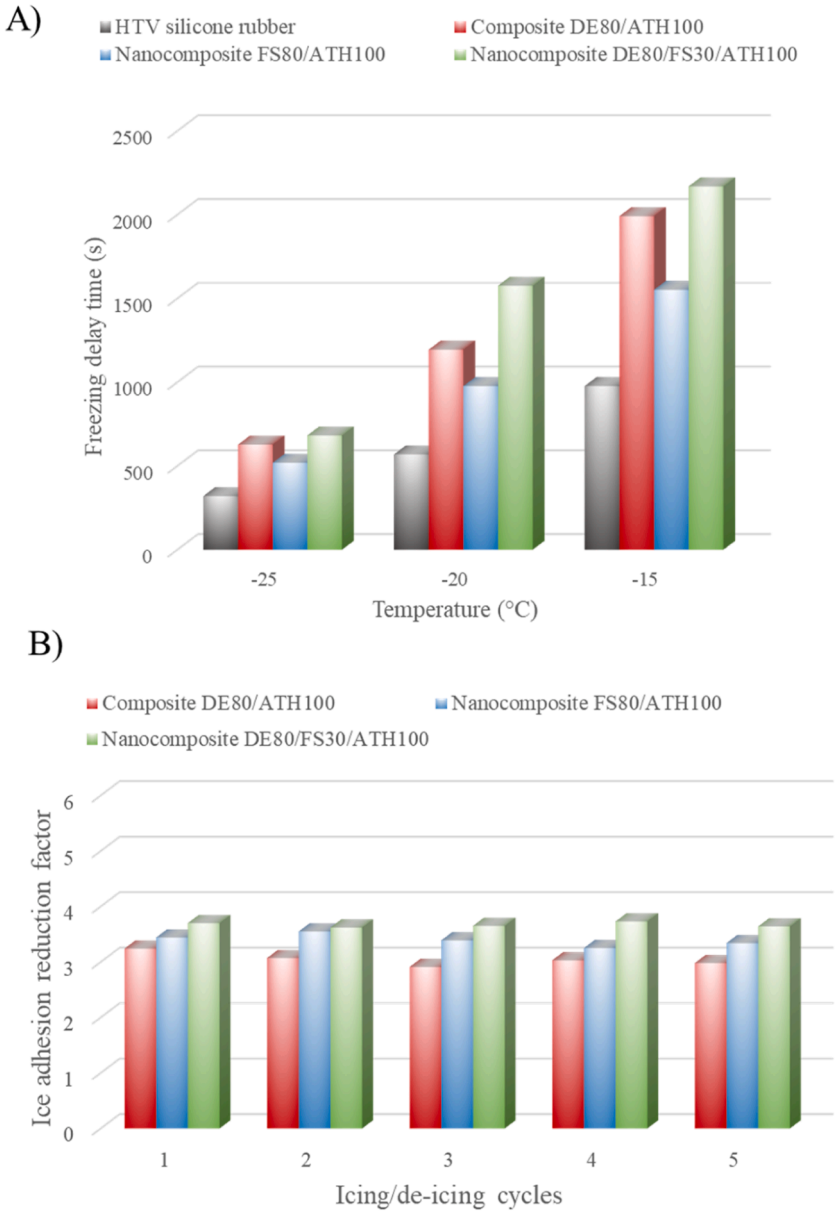

Fig. 7. A) Freezing delay time at various temperatures; B) Ice adhesion reduction factor as a function of icing/de-icing cycles.

persistent through five icing/de-icing cycles testifying the durability of the developed materials against repetitive de-icing processes.

3.6. Mechanochemical stability and hydrophobic recovery

Mechanochemical durability of the superhydrophobic surfaces is one of their main drawbacks which restricts their practical application. In this paper, to address this concern, we developed a mechanochemically stable ultra-robust superhydrophobic bulk materials. In terms of the mechanical and adhesion durability, several tests were conducted on the as-produced materials including sand-paper abrasion, tape-peeling, cutter scratching, and dynamic impact stability. The schematics and related figures and images of these analyses are presented in Fig. 8. The abrasion durability is performed by abrading the materials by various sandpapers. The alteration in the water CA and CAH of the samples after abrasion for 5000 cm distance is illustrated in Fig. 8(A-1). Among the produced samples, the nanocomposite FS80/ATH100 showed considerable enhancement in its non-wetting attributes after abrasion which can be related to the presence of pronounced microstructures covered with nano-scale features on its abraded surface. By changing the sandpapers from rough to fine, whilst the CAH values of the abraded materials were relatively unchanged, a slight decreasing trend in the water CA was observed that can signify the importance of the size of micro-scale surface roughness on the spherical shape of the static water droplet. Over the whole range of sandpaper grade numbers, all samples retained superhydrophobicity which indicates their abrasion-insensitive water-repellent behavior. For gaining more information on their resistivity against sandpaper, the retention ratio of the developed materials after abrasion was also measured (supplementary materials Table S1). The retention ratio (η) is defined as the ratio between sample weight after abrasion (m_2) to its original weight (m_1) ($\eta = m_2 / m_1$) [41]. Among the developed samples, the highest retention ratio was achieved for the composite DE80/ATH100 indicating its minimal number of worn debris. This can be resulted from the highest hardness and the condensed form of the composite compared to the two of the nanocomposites which leads to its high retention ratio. As another effective factor during practical application, we examined the cohesiveness of the materials using tape-peeling test with a scotch tape. The materials were subjected to repetitive adhesion/peel-off cycles. The negligible changes of the water CA and CAH over 150 cycles ascertained the strong cohesive forces among the matrix and incorporated particles (Fig. 8(B)).

Since all the produced materials demonstrated practically identical behavior against mechanical stability measurements, we performed further mechanical studies including cutter scratching and dynamic impact tests on the composite DE80/ATH100 as the representative of the superhydrophobic bulk materials. As illustrated in Fig. 8(C), the scratched surface maintained the water repellency. As a more vigorous yet practical set of experiments, we implemented a combination of mechanical tests in a sequential manner, i.e., knife scratching, finger touching, hammer beat, and tape peeling tests (see supplementary Video S). After these series of experiments, the as-prepared composite preserved its superhydrophobicity and roll off properties. The dynamic impact durability tests are crucial for outdoor applications due to the susceptibility of the fragile surface structures of superhydrophobic materials to impact damages. Here, we performed these tests under both liquid and solid phases each of which imitates a specific outdoor condition of the precipitation and collision of pollutions with the surface respectively (Fig. 8(D) and Fig. 8(E)). After 10 min, the water repellency was unchanged showing water CA $>160^\circ$ and CAH $<5^\circ$ Regarding solid impact durability test, the tilted surface was bombarded with SiC particles from the same height. We selected silicon carbide particles due to their resemblance in shape, size, and hydrophilicity to natural pollutant. In order to clean the contaminated surface, we employed a syringe to flow a water jet over the surface. As illustrated in Fig. 8(E), the SiC particles were easily adhered to the water jet and were taken away. Finally, the surface became completely clean and remained water repellent like its original state.

Chemical stability is another vital factor affecting the application of superhydrophobic surfaces in practical situations. The stability of the developed materials was assessed against acid/alkali solutions and UV radiation. As shown in Fig. 9(A), the samples were submerged in aqueous media having pH values of 4, 7, and 10 for 48 hr. Then, the water CA and CAH of the samples before and after immersion were measured. After 48 h of continuous contact with aqueous solutions, the water CA and CAH of the materials remained relatively unaffected verifying their superb resistance against chemical solutions and the stability of the Cassie-Baxter regime on these materials. UV resistance is of great importance for materials used in outdoor applications such as electrical insulators. Thus, the produced composite and nanocomposites were exposed to UV radiation in an accelerated universal weathering system for 300 h where samples were periodically removed from the chamber every 100 h to measure their water CA and CAH (Fig. 9(B)). Due to the great binding energy of the $(SiO)_x$ chemical groups of silicone rubber, the samples retained water repellency after 300 h continuous exposure to UV light. These observations confirmed their outstanding stability against UV radiation.

One of the appealing abilities of silicone rubber is called hydrophobic recovery which corresponds to repetitive retrieval of its hydrophobic properties following alteration in its surface energy. Depending on the nature of its modified surface, hydrophobic recovery may stem from different physical and chemical processes including diffusion of uncrosslinked low molecular weight siloxane (LMWS) chains from the bulk to the surface, thermodynamically favorable reorientation of polar groups from the surface to the bulk phase or nonpolar groups from the bulk to the surface, and condensation of the surface hydroxyl groups [71]. Since the incorporation of micro and/or nano-sized particles may affect the hydrophobic recovery procedure, we studied the alteration in water CA of produced materials over time after multiple flashover tests. As illustrated in Fig. 9(C), the non-wettability characteristic of the substrates was changed after 20 times of dry flashover. The water CA of the materials was $<50^\circ$ showing the hydrophilic nature of the surface. Due to the oxidation of methyl groups with oxygen surrounded the samples during flashover, a hydrophilic layer containing hydroxyl groups covers the surface which is more prominent around the high voltage electrode. It takes at least 10 days for the materials to recover their hydrophobicity which is prolonged due to the restriction effect of particles embedded within silicone rubber. Comparing the results of composite and nanocomposites revealed considerable hindrance impact of nano-sized fumed silica than micro-sized particles on the speed of surface hydrophobic recovery where the nanocomposite FS80/ATH100 did not achieve water CA $>150^\circ$ after 20 days. However, composite DE80/ATH100 and nanocomposite DE80/FS30/ATH100 showed acceptable hydrophobic recovery properties.

3.7. Radar diagram

To give an outline of the characteristics of the produced materials and compare them with unfilled HTV silicone rubber, the radar diagrams are utilized to assess the experimental results. The rating system is designed based on the performance of the materials and their average values in diverse analyses. The rating of each characteristic and the associated average values of the produced materials are presented in the supplementary materials (Table S2-S5). Each characteristic is graded from 1 to 10 where 10 corresponds to the best performance and 1 represents the worst. Thus, the larger the surface area of the diagram, the better the functionality of the developed material. As illustrated in Fig. 10, various properties are presented in these diagrams including surface and bulk CA, surface and bulk CAH, CA after abrasion, CAH after abrasion, hardness, dielectric loss, flashover voltage, freezing delay time, ARF, and hydrophobic recovery. By the incorporation of particles, we observed substantial enhancement in all the surface and bulk properties of the materials than unfilled silicone rubber except for the

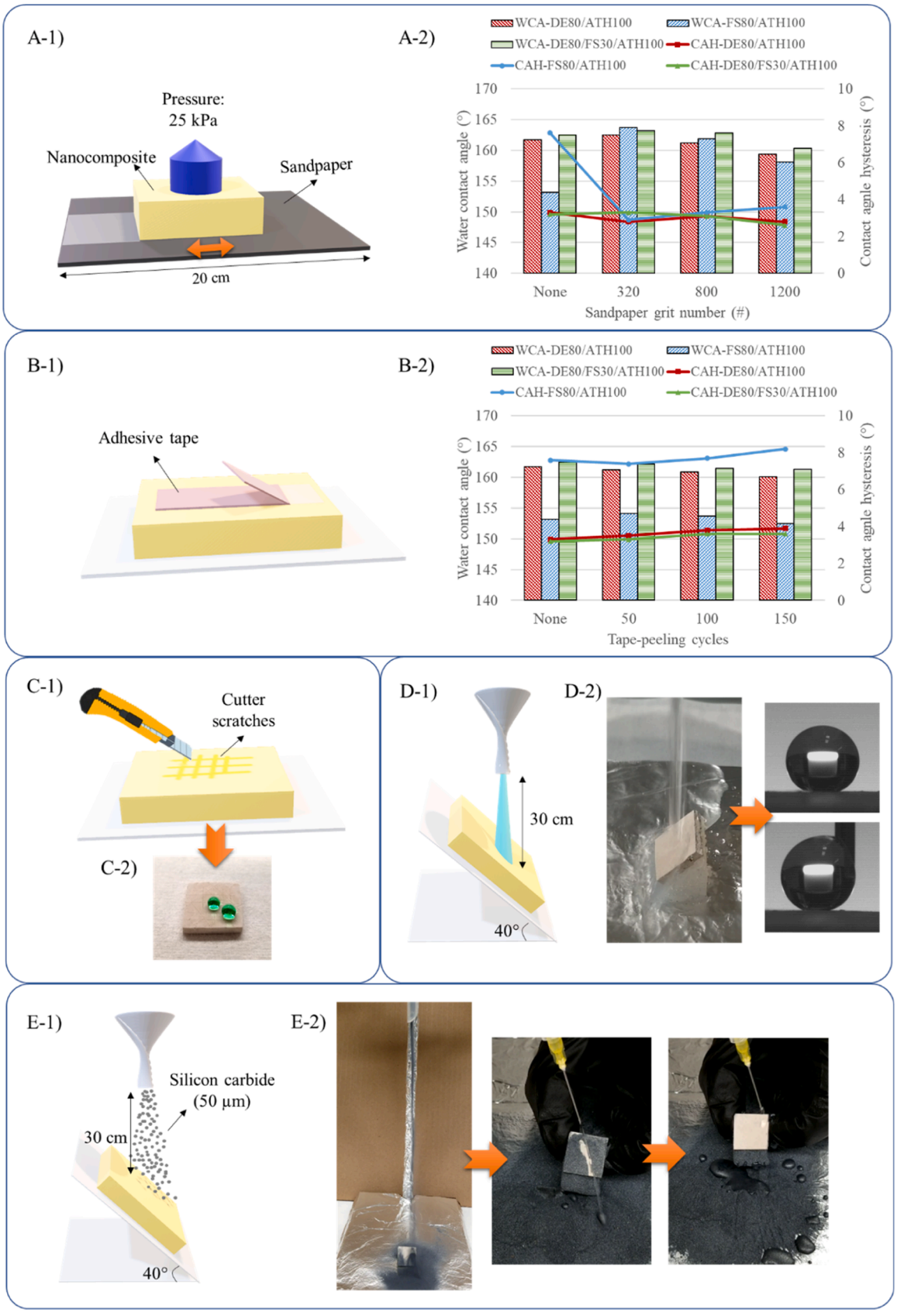

Fig. 8. The schematic and the alteration in the water CA and CAH of the samples after A) abrasion for 5000 cm distance using various sandpaper grit numbers; B) tape peeling cycles; C) cutter scratching and D) water jet impact and the state of the water droplets on the surface; E) Bombardment with SiC particles and self-cleaning property.

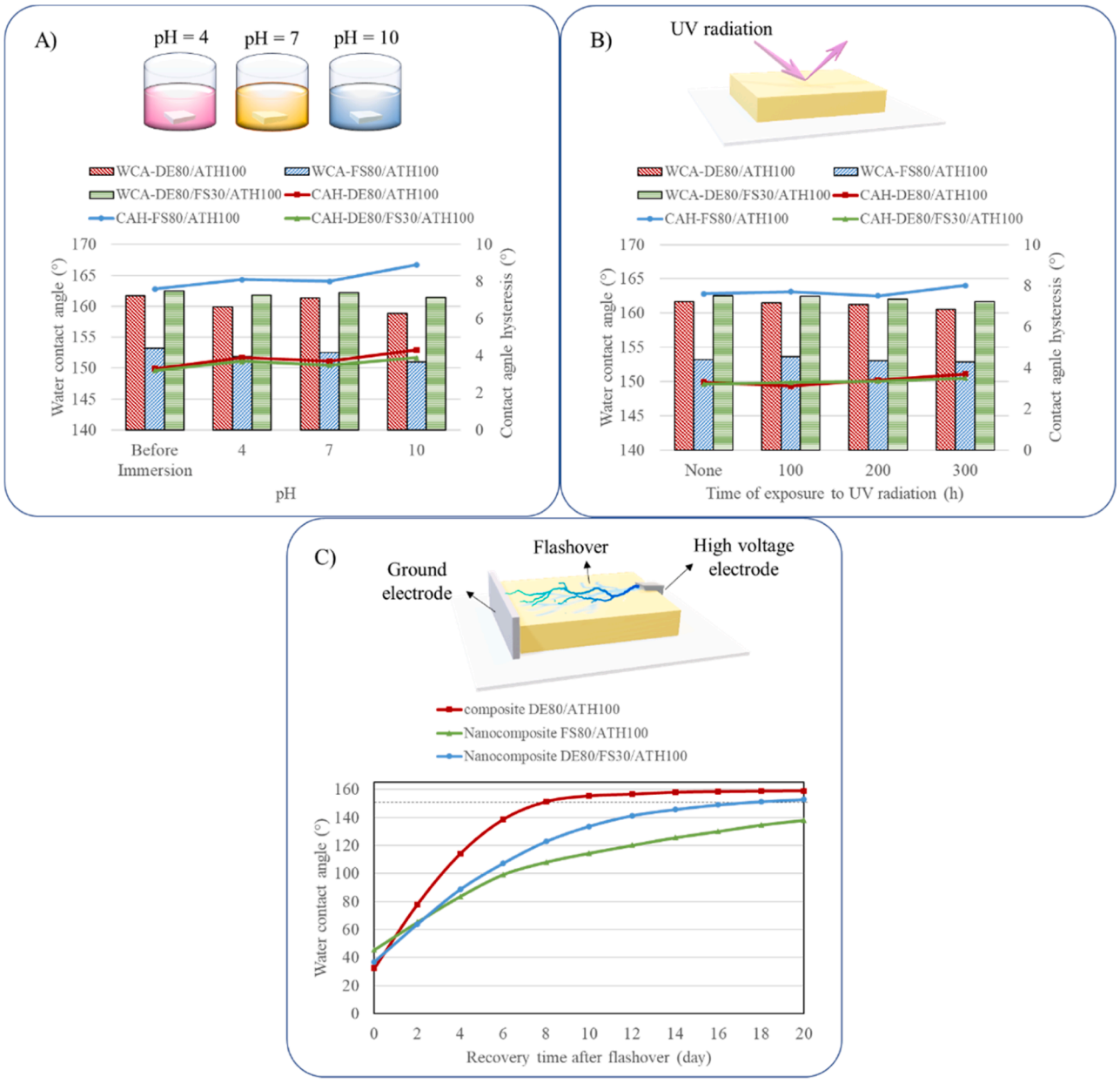

Fig. 9. Water CA and CAH of the samples after A) 48 hr submersion in solution with various pH values; B) 300 hr exposure to UV radiation; C) 20 times high voltage flashovers.

dielectric loss and hydrophobic recovery which resulted from having filler content higher than percolation threshold. The quaternary nanocomposite of DE80/FS30/ATH100 possessed the highest surface and bulk water repellency before and after abrasion and better icephobic properties. The composite of DE80/ATH100, however, showed the best performance in hydrophobic recovery and dry flashover voltages.

4. Conclusions

Three silicone micro and nanocomposites were produced using diatomaceous earth (DE), fumed silica (FS) and alumina trihydrate (ATH) particles to achieve desirable bulk superhydrophobicity, physical properties, mechanical and chemical durability, hydrophobic recovery, electrical properties, and icephobicity. All composites acquired superhydrophobic properties both on the surface and bulk of their materials with a slight difference in the CAH (with a maximum CA of 162.5° and minimum CAH of 3.2°). The addition of DE particles resulted in delayed second weight loss step and a broadened range of decomposition temperature (almost 90°) with lower weight loss rate. The incorporation of nanoparticles significantly enhanced the icephobic properties across all tests due to the formation of micro-nanostructures throughout the material. Among all the samples tested, the nanocomposite FS80/ATH100 failed to recover its superhydrophobic properties after the high-voltage flashover test. This was attributed to the greater hindrance effect of nano-sized fumed silica compared to micro-sized particles on the rate of surface hydrophobic recovery. The composite of DE80/ATH100 and nanocomposite of DE80/FS30/ATH100 showed enhanced properties in all aspects. While the composite of DE80/ATH100 showed a better performance in hydrophobic recovery and flashover voltage, the quaternary nanocomposite of DE80/FS30/ATH100 showed better icephobicity and durability after mechanical abrasion. The results of this study can help selecting an enhanced composite to serve better for the environment and application that the material is designed to be used.

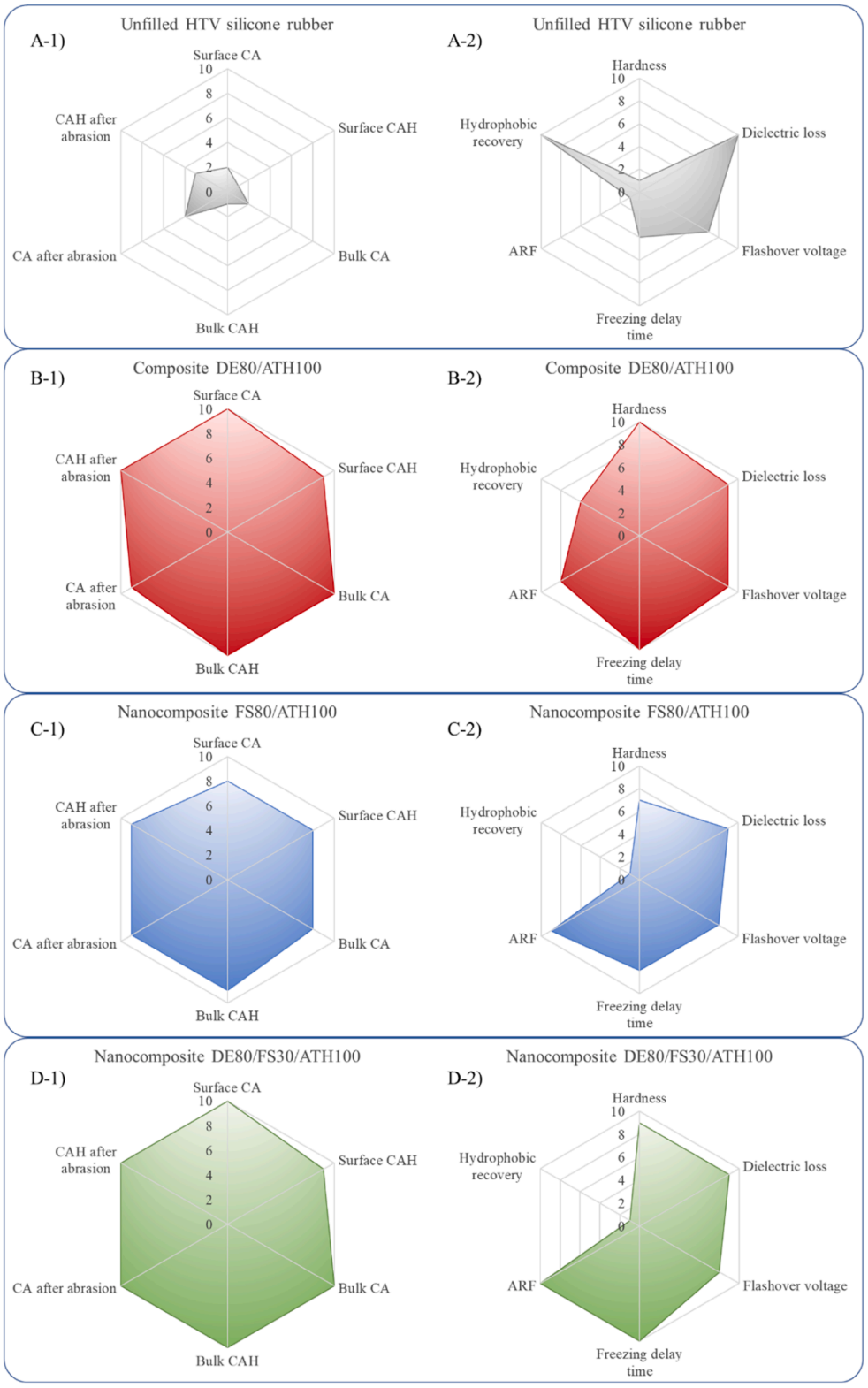

Fig. 10. Radar diagram to compare the performance of all developed materials in terms of non-wettability properties and physical, electrical, and icephobic properties.

CRediT authorship contribution statement

Elham Vazirinasab: Writing – review & editing, Writing – original draft, Visualization, Validation, Supervision, Methodology, Data curation. **Khosrow Maghsoudi:** Writing – review & editing, Validation, Methodology. **Gelareh Momen:** Visualization, Validation, Supervision, Project administration. **Reza Jafari:** Visualization, Validation, Supervision, Project administration, Funding acquisition.

Declaration of competing interest

The authors declare that they have no known competing financial

interests or personal relationships that could have appeared to influence the work reported in this paper.

Acknowledgments

The authors gratefully acknowledge the financial support provided by Mitacs.We would also like to thank Mohammad Bakhtiari for his assistance with the graphical abstract. Our sincere thanks go to the Laboratory of Icephobic Coatings and Surface Engineering (LaRGIS) at the Université du Québec à Chicoutimi (UQAC) for providing the necessary equipment and materials used in this research.

Supplementary materials

Supplementary material associated with this article can be found, in the online version, at doi:10.1016/j.rineng.2025.108623.

Data availability

Data will be made available on request.

References

[1] S. Xu, Y. Zhang, T. Wang, Recent developments of femtosecond laser direct writing for Meta-Optics, Nanomaterials 13 (5) (2023), https://doi.org/10.3390/nano13050872.
[2] M.H. Syed, A. Bhat, M. Amin, et al., Recent progress in biopolymer-based electrospun nanofibers and their biomedical applications, Eur. Polym. J. 188 (2023), https://doi.org/10.1016/j.eurpolymj.2023.112071.
[3] A. Kanioura, V. Constantoudis, P. Petrou, D. Kletsas, A. Tserepi, E. Gogolides, M. Chatzichristidi, S. Kakabakos, Oxygen plasma micro-nanostructured PMMA plates and microfluidics for increased adhesion and proliferation of cancer versus normal cells: the role of surface roughness and disorder, Micro Nano Eng. 8 (March) (2020) 100060, https://doi.org/10.1016/j.mne.2020.100060.
[4] Y. Zhang, L. Zhang, K. Cui, Sh. Ge, X. Cheng, M. Yan, J. Yu, H. Liu, Flexible electronics based on micro/nanostructured paper, Adv. Mater. 30 (51) (2018) 1–39, https://doi.org/10.1002/adma.201801588.
[5] K. Maghsoudi, R. Jafari, G. Momen, M. Farzaneh, Micro-nanostructured polymer surfaces using injection molding: a review, Mater. Today Commun. 13 (2017) 126–143, https://doi.org/10.1016/j.mtcomm.2017.09.013.
[6] K. Maghsoudi, E. Vazirinasab, G. Momen, R. Jafari, Advances in the fabrication of superhydrophobic polymeric surfaces by polymer molding processes, Ind. Eng. Chem. Res. 59 (20) (2020) 9343–9363, https://doi.org/10.1021/acs.iecr.0c00508.
[7] E. Vazirinasab, R. Jafari, G. Momen, Application of superhydrophobic coatings as a corrosion barrier: a review, Surf. Coat. Technol. 341 (October 2017) (2018) 40–56, https://doi.org/10.1016/j.surfcoat.2017.11.053.
[8] G. Wang, A. Li, K. Li, Y. Zhao, Y. Ma, Q. He, A fluorine-free superhydrophobic silicone rubber surface has excellent self-cleaning and bouncing properties, J. Colloid. Interface Sci. 588 (2021) 175–183, https://doi.org/10.1016/j.jcis.2020.12.059.
[9] D. Wang, et al., Design of robust superhydrophobic surfaces, Nature 582 (7810) (2020) 55–59, https://doi.org/10.1038/s41586-020-2331-8.
[10] M. Yaghoubi, N.P. Ahmadi, S. Yazdani, Fabrication of robust superhydrophobic zinc-coated steel with anti-corrosion and self-cleaning behavior through a simple nickel galvanic replacement reaction, Colloids. Surf. a Physicochem. Eng. Asp. 686 (Avril) (2024) 150192, https://doi.org/10.1016/j.colsurfa.2024.133341.
[11] G.M. M S Koochaki, R.J. S Lavoie, Enhancing icephobic coatings: exploring the potential of dopamine-modified epoxy resin inspired by mussel catechol groups, Biomimetics. 9 (6) (2024) 349, https://doi.org/10.3390/biomimetics9060349.
[12] K. Maghsoudi, et al., The thermodynamic stability of the Cassie–Baxter regime determined by the geometric parameters of hierarchical superhydrophobic surfaces, Appl. Mater. Today. 34 (October) (2023) 1610–1619, https://doi.org/10.1016/j.apmt.2023.101893.
[13] V. Selvaraj, T. Swarna Karthika, C. Mansiya, V. Andal, M. Alagar, Review on superhydrophobic polymer composite coating materials and its coating technology for advanced applications, Polym.-Plast. Tech. Mater. 64 (2025) 694–734, https://doi.org/10.1080/25740881.2024.243122017.
[14] V.A. Ganesh, H.K. Raut, A.S. Nair, S. Ramakrishna, A review on self-cleaning coatings, J. Mater. Chem. 21 (41) (2011) 16304–16322, https://doi.org/10.1039/c1jm12523k.
[15] J. Song, Y. Li, W. Xu, H. Liu, Y. Lu, Inexpensive and non-fluorinated superhydrophobic concrete coating for anti-icing and anti-corrosion, J. Colloid. Interface Sci. 541 (2019) 86–92, https://doi.org/10.1016/j.jcis.2019.01.014.
[16] R. Han, Z. Han, X. Song, W. Cui, P. Jin, G. Dong, K. Niu, Hydrophilic silica transformed silicone rubber into superhydrophobic composites, Polym. Compos. 45 (1) (2023) 873–881, https://doi.org/10.1002/pc.27822.
[17] L. Zhang, H. Zhao, L. Zhu, Investigation on improving mechanical property of silicone rubber by employing functionalised nanosilica, J. Chem. Res. 48 (3) (2024), https://doi.org/10.1177/17475198241260559.
[18] N. Kavitha, J. Dhivakar, N. Bhavani, R. Sarathi, S. Kornhuber, Understanding the impact of different nanofillers on electrical, thermal, and surface properties of corona-aged silicone rubber nanocomposites, Polym. Compos. 46 (2) (2024) 1686–1698, https://doi.org/10.1002/pc.29065.
[19] P.B. Lie Chen, H. Ping, T. Yang, T. Hu, Icing performance of superhydrophobic silicone rubber surfaces by laser texturing, Mater. Res. Express. 6 (2019), https://doi.org/10.1088/2053-1591/ab6542.
[20] K. Maghsoudi, E. Vazirinasab, G. Momen, R. Jafari, Icephobicity and durability assessment of superhydrophobic surfaces: the role of surface roughness and the ice adhesion measurement technique, J. Mater. Process. Technol. 288 (July 2020) (2021) 116883, https://doi.org/10.1016/j.jmatprotec.2020.116883.
[21] J. Tan, A.C.C. Esteves, J. Yang, S. Zhou, Zwitterion-bearing silica sol for enhancing antifouling performance and mechanical strength of transparent PDMS coatings, Prog. Org. Coat. 191 (2024) 108415, https://doi.org/10.1016/j.porgcoat.2024.108415. June.
[22] M.S. Selim a, N.A. Fatthallah, Sh.A. Higazy, Z. Hao, Chem. Eng. Sci. 304 (2025) 121083, https://doi.org/10.1016/j.ces.2024.121083, 1 February.
[23] M.S. Selim, Sh.A. El-Safty, M.A. Shenashen, A. Elmarakbi, Advances in polymer/inorganic nanocomposite fabrics for lightweight and high-strength armor and ballistic-proof materials, Chem. Eng. J. 493 (2024) 152422, https://doi.org/10.1016/j.cej.2024.152422, 1 August.
[24] M.S. Selim, N.A. Fatthallah, Sh.A. Higazy, Z.H W.Zhuorui, Superhydrophobic silicone/graphene oxide-silver-titania nanocomposites as eco-friendly and durable maritime antifouling coatings, Ceram. Int. Vol. 50 (Issue 1) (2024) 452–463, https://doi.org/10.1016/j.ceramint.2023.10.121. Part A1 January.
[25] J. Chen, X. Chen, Z. Hao, Z. Wu, M.S. Selim, J. Yu, Y. Huang, Robust and superhydrophobic polydimethylsiloxane/Ni@ti$_3$c$_2$t$_x$ nanocomposite coatings with assembled eyelash-like microstructure array: a new approach for effective passive anti-icing and active photothermal deicing, ACS. Appl. Mater. Interfaces. 16 (Issue 20) (2024), https://doi.org/10.1021/acsami.4c01561.
[26] R. Ghamarpoor, M. Jamshidi, Preparation of superhydrophobic/superoleophilic nitrile rubber nanocomposites containing silanized nano silica for efficient oil/water separation, Sep. Purif. Technol. 292 (2022). Article 120854.
[27] R. Ghamarpoor, M. Jamshidi, M. Sayyadian, M. Razavizadeh, Effects of chemical/photochemical functionalization of polyethylene terephthalate fabric on mechanical properties and bonding to nitrile rubber, Sci. Rep. 13 (2023), https://doi.org/10.1016/j.arabjc.2023.105098. Article 41432.
[28] G. Wang, A.Li, W.Z, Z. Xu, Y. Ma, F. Zhang, Y. Zhang, J. Zhou, Q. He, "A review on fabrication methods and research progress of superhydrophobic silicone rubber materials," vol. 2001460, pp. 1–19, 2021, doi: 10.1002/admi.202001460.
[29] Y. Zhao, Y. Xiang, S. Gu, B. Du, B. Dong, N. Xiang, H. Xu, Effect of surface roughness on flashover characteristics of silicone rubber, J. Electrostat. 99 (January) (2019) 41–48, https://doi.org/10.1016/j.elstat.2019.04.004.
[30] Y. Li, H. Jin, S. Nie, P. Zhang, N. Gao, Dynamic behavior of water droplets and flashover characteristics on a superhydrophobic silicone rubber surface, Appl. Phys. Lett. 110 (20) (2017), https://doi.org/10.1063/1.4983714.
[31] E. Vazirinasab, R. Jafari, G. Momen, Wetting and self-cleaning properties of silicone rubber surfaces treated by atmospheric plasma jet, Annu. Rep. - Conf. Electr. Insul. Dielectr. Phenom., CEIDP 2018-Octob (2018) 239–242, https://doi.org/10.1109/CEIDP.2018.8544835.
[32] M. Zhao, W. Li, Y. Wu, X. Zhao, M. Tan, J. Xing, Performance investigation on different designs of superhydrophobic surface texture for composite insulator, Materials 12 (7) (2019) 1164, https://doi.org/10.3390/ma12071164.
[33] G. Wang, J. Zhou, Y. Zhang, Y. Zhang, Q. He, A superhydrophobic surface with aging resistance, excellent mechanical restorability and droplet bounce properties, Soft. Matter. 16 (23) (2020) 5514–5524.
[34] M. Zhu, H. Song, J. Li, J. Xue, Q. Yu, J. Chen, Superhydrophobic and high-flashover-strength coating for HVDC insulating system, Chem. Eng. J. 404 (May 2020) (2021) 126476, https://doi.org/10.1016/j.cej.2020.126476.
[35] G. Momen, M. Farzaneh, Survey of micro/nano filler use to improve silicone rubber for outdoor insulators, Rev. Adv. Mater. Sci. 27 (1) (2011) 1–13.
[36] A.C. Ribeiro, "Superhydrophobic nanostructured coatings for electrical insulators," no. November 2019, pp. 2557–2567, 2020, doi: 10.1002/pc.25554.
[37] S.A. Seyedmehdi, H. Zhang, J. Zhu, Superhydrophobic RTV silicone rubber insulator coatings, Appl. Surf. Sci. 258 (7) (2012) 2972–2976, https://doi.org/10.1016/j.apsusc.2011.11.020.
[38] A. Li, G. Wang, Y. Ma, C. Zhao, F. Zhang, Q. He, F. Zhang, Study on preparation and properties of superhydrophobic surface of RTV silicone rubber, J. Mater. Res. Technol. 11 (2021) 135–143, https://doi.org/10.1016/j.jmrt.2020.12.074.
[39] S.P. Dalawai, M.A.S. Aly, S.S. Latthe, R. Xing, R.S. Sutar, S. Nagappan, C.-S. Ha, K. K. Sadasivuni, S. Liu, Recent advances in durability of superhydrophobic self-cleaning technology: a critical review, Prog. Org. Coat. 138 (May 2019) (2020) 105381, https://doi.org/10.1016/j.porgcoat.2019.105381.
[40] K. Tu, X. Wang, L. Kong, H. Chang, J. Liu, Fabrication of robust, damage-tolerant superhydrophobic coatings on naturally micro-grooved wood surfaces, RSC. Adv. 6 (2015) 701–707, https://doi.org/10.1039/C5RA24407B.
[41] X. Zhang, D. Zhi, L. Sun, Y. Zhao, M.K. Tiwari, C.J. Carmalt, I.P. Parkinc, Y. Lu, Super-durable, non-fluorinated superhydrophobic free-standing items, J. Mater. Chem. A 6 (2) (2017) 357–362, https://doi.org/10.1039/c7ta08895g.
[42] E.K. Sam, D.K. Sam, X. Lv, B. Liu, X. Xiao, S. Gong, W. Yu, J. Chen, J. Liu, Recent development in the fabrication of self-healing superhydrophobic surfaces, Chem. Eng. J. 373 (March) (2019) 531–546, https://doi.org/10.1016/j.cej.2019.05.077.
[43] S. Liu, W. Wan, X. Zhang, A. De Crema, S. Seeger, All-organic fluorine-free superhydrophobic bulk material with mechanochemical robustness and photocatalytic functionality, Chem. Eng. J. 385 (December 2019) (2020) 123969, https://doi.org/10.1016/j.cej.2019.123969.

[44] X. Zhang, Y. Guo, H. Chen, W. Zhu, P. Zhang, A novel damage-tolerant superhydrophobic and superoleophilic material, J. Mater. Chem. A 2 (24) (2014) 9002, https://doi.org/10.1039/c4ta00869c.
[45] Ch. Chen, M. Liu, Y. Hou, L. Zhang, M. Li, D. Wang, S. Fu, Microstructure-controllable nanocomplexes bulk possessed with durable superhydrophobicity, Chem. Eng. J. 389 (October 2019) (2020) 124420, https://doi.org/10.1016/j.cej.2020.124420.
[46] S. Liu, X. Zhang, S. Seeger, Tunable bulk material with robust and renewable superhydrophobicity designed via in-situ loading of surface-wrinkled microparticles, Chem. Eng. J. 408 (October 2020) (2021) 127301, https://doi.org/10.1016/j.cej.2020.127301.
[47] E. Vazirinasab, G. Momen, R. Jafari, A non-fluorinated mechanochemically robust volumetric superhydrophobic nanocomposite, J. Mater. Sci. Technol. 66 (2021) 213–225, https://doi.org/10.1016/j.jmst.2020.06.029.
[48] V.T. Ambegoda and S.M. Egodage, "Enhancement of hydrophobicity of natural rubber latex films using diatomaceous earth," no. May, pp. 1–7, 2020, doi: 10.1002/app.50047.
[49] E. Vazirinasab, R. Jafari, G. Momen, Evaluation of atmospheric-pressure plasma parameters to achieve superhydrophobic and self-cleaning HTV silicone rubber surfaces via a single-step, eco-friendly approach, Surf. Coat. Technol. 375 (July) (2019) 100–111, https://doi.org/10.1016/j.surfcoat.2019.07.005.
[50] M. Ehsani, H. Borsi, E. Gockenbach, G.R. Bakhshandeh, J. Morshedian, Modified silicone rubber for use as high voltage outdoor insulators, Adv. Polym. Technol. 24 (1) (2005) 51–61, https://doi.org/10.1002/adv.20027.
[51] K. Baek, H. Shin, M. Cho, Multiscale modeling of mechanical behaviors of Nano-SiC/epoxy nanocomposites with modified interphase model: effect of nanoparticle clustering, Compos. Sci. Technol. 203 (2021).
[52] V.P. Silva, M.P. Paschoalino, M.C. Gonçalves, M.I. Felisberti, W.F. Jardim, I.V. P. Yoshida, Silicone rubbers filled with TiO2: characterization and photocatalytic activity, Mater. Chem. Phys. 113 (1) (2009) 395–400, https://doi.org/10.1016/j.matchemphys.2008.07.104.
[53] M.T. Nazir, B.T. Phung, S. Yu, Y. Zhang, and S. Li, "Tracking, erosion and thermal distribution of micro-AlN + nano-SiO co-filled silicone rubber for high-voltage outdoor insulation," vol. 3, pp. 289–294, 2018, doi: 10.1049/hve.2018.5033.
[54] Y. Jeon, S.K. Hong, M. Kim, Effect of filler concentration on tracking resistance of ATH-filled silicone rubber nanocomposites, Energies 12 (12) (2019), https://doi.org/10.3390/en12122401.
[55] S. Ilhan, D. Tuzun, A. Ozdemir, Comparative properties of HTV silicone rubber for composite insulators - ATH and silica fillers, IEEe Trans. Dielectr. Electr. Insul. 28 (2) (2021) 414–422.
[56] Y. Tian, Z. Yuan, X. Huang, C. Liu, S. Li, D. Lu, High-efficiency enhancement of the surface weatherability and electrical and mechanical properties of a cycloaliphatic epoxy-based hybrid nanocomposite via reaction-induced organic functional groups, Prog. Org. Coat. 148 (May) (2020) 105830, https://doi.org/10.1016/j.porgcoat.2020.105830.
[57] I. Ramirez, E.A. Cherney, S. Jarayam, Comparison of the erosion resistance of silicone rubber and EPDM composites filled with micro silica and ATH, IEEe Trans. Dielectr. Electr. Insul. 19 (1) (2012) 218–224, https://doi.org/10.1109/TDEI.2012.6148521.
[58] Y. Lin, L. Wang, F. Yin, M. Farzaneh, Y. Liu, S. Gao, Comparison of four commonly used high temperature vulcanized silicone rubber formulas for outdoor insulator and their regional adaptability, J. Appl. Polym. Sci. 47477 (2019) 47477, https://doi.org/10.1002/app.47477.
[59] Z. Zhijin, L. Tian, J. Xingliang, L. Chen, Y. Shenghuan, Z. Yi, Characterization of silicone rubber degradation under salt-fog environment with AC test voltage, IEEe Access. 7 (2019) 66714–66724, https://doi.org/10.1109/ACCESS.2019.2917700.
[60] S. He, J. Hu, C. Zhang, J. Wang, L. Chen, X. Bian, J. Lin, X. Du, Performance improvement in nano-alumina filled silicone rubber composites by using vinyl trimethoxysilane, Polym. Test. 67 (February) (2018) 295–301, https://doi.org/10.1016/j.polymertesting.2018.03.023.
[61] Y. Xue, X. fei Li, D. hai Zhang, H. sheng Wang, Y. Chen, Y. fa Chen, Comparison of ATH and SiO2 fillers filled silicone rubber composites for HTV insulators, Compos. Sci. Technol. 155 (2018) 137–143, https://doi.org/10.1016/j.compscitech.2017.12.006.
[62] I. Pleşa, P.V. Noţingher, S. Schlögl, C. Sumereder, M. Muhr, Properties of polymer composites used in high-voltage applications, Polymers. (Basel) 8 (5) (2016), https://doi.org/10.3390/polym8050173.
[63] K.A. Page and K. Adachi, "Dielectric relaxation in montmorillonite/polymer nanocomposites," vol. 47, pp. 6406–6413, 2006, doi: 10.1016/j.polymer.2006.06.042.
[64] Y. Zhao, et al., Effect of surface roughness on flashover characteristics of silicone rubber, J. Electrostat. 99 (May) (2019) 41–48, https://doi.org/10.1016/j.elstat.2019.04.004.
[65] Y. Shen, et al., Spraying fabrication of durable and transparent coatings for anti-icing application: dynamic water repellency, icing delay, and ice adhesion, ACS. Appl. Mater. Interfaces. 11 (3) (2019) 3590–3598, https://doi.org/10.1021/acsami.8b19225.
[66] H. Wang, et al., Bouncing behavior of a water droplet on a super-hydrophobic surface near freezing temperatures, Int. J. Heat. Mass Transf. 174 (2021) 121304, https://doi.org/10.1016/j.ijheatmasstransfer.2021.121304.
[67] T.B. Nguyen, S. Park, H. Lim, Effects of morphology parameters on anti-icing performance in superhydrophobic surfaces, Appl. Surf. Sci. 435 (2018) 585–591, https://doi.org/10.1016/j.apsusc.2017.11.137.
[68] A.A. Yancheshme, G. Momen, R.J. Aminabadi, Mechanisms of ice formation and propagation on superhydrophobic surfaces : a review, Adv. Colloid. Interface Sci. 279 (2020) 102155, https://doi.org/10.1016/j.cis.2020.102155.
[69] E. Vazirinasab, K. Maghsoudi, R. Jafari, G. Momen, A comparative study of the icephobic and self-cleaning properties of Teflon materials having different surface morphologies, J. Mater. Process. Technol. 276 (2020) 116415, https://doi.org/10.1016/j.jmatprotec.2019.116415.
[70] E.A. Cherney, "Silicone rubber dielectrics modified by inorganic fillers for outdoor high voltage insulation applications," vol. 12, no. 6, pp. 1108–1115, 2005.
[71] E. Bormashenko, G. Chaniel, R. Grynyov, Towards understanding hydrophobic recovery of plasma treated polymers: storing in high polarity liquids suppresses hydrophobic recovery, Appl. Surf. Sci. 273 (2013) 549–553, https://doi.org/10.1016/j.apsusc.2013.02.078.